

---

# Equivariant Spherical Transformer for Efficient Molecular Modeling

---

**Junyi An\***  
SAIS  
anjunyi@sais.com.cn

**Xinyu Lu\*†**  
Shanghai Innovation Institute  
Xiamen University  
xinyulu@stu.xmu.edu.cn

**Chao Qu‡**  
INFTECH  
quchao\_tequila@inftech.ai

**Yunfei Shi**  
SAIS  
shiyunfei@sais.com.cn

**Peijia Lin†**  
Sun Yat-sen University  
Shanghai Innovation Institute  
linpj6@mail2.sysu.edu.cn

**Qianwei Tang†**  
Nanjing University  
cleveland225@163.com

**Licheng Xu**  
SAIS  
xulicheng@sais.com.cn

**Fenglei Cao‡**  
SAIS  
caofenglei@sais.com.cn

**Yuan Qi‡**  
SAIS  
Fudan University  
Zhongshan Hospital  
qiyuan@fudan.edu.cn

## Abstract

Equivariant Graph Neural Networks (GNNs) have significantly advanced the modeling of 3D molecular structure by leveraging group representations. However, their message passing, heavily relying on Clebsch-Gordan tensor product convolutions, suffers from restricted expressiveness due to the limited non-linearity and low degree of group representations. To overcome this, we introduce the Equivariant Spherical Transformer (EST), a novel plug-and-play framework that applies a Transformer-like architecture to the Fourier spatial domain of group representations. EST achieves higher expressiveness than conventional models while preserving the crucial equivariant inductive bias through a uniform sampling strategy of spherical Fourier transforms. As demonstrated by our experiments on challenging benchmarks like OC20 and QM9, EST-based models achieve state-of-the-art performance. For the complex molecular systems within OC20, small models empowered by EST can outperform some larger models and those using additional data. In addition to demonstrating such strong expressiveness, we provide both theoretical and experimental validation of EST’s equivariance as well, paving the way for new research in this area.

## 1 Introduction

Graph neural networks (GNNs) are increasingly used for modeling molecular systems and approximating quantum mechanical calculations, providing crucial support for computational chemistry tasks like drug discovery [1] and material design [2]. Compared to traditional methods such as

---

\*equal contribution. SAIS: Shanghai Academy of AI for Science

†This work is done when they are interns at SAIS

‡corresponding authors: Fenglei Cao is the corresponding author in SAIS, and Chao Qu is the corresponding author in INFLY TECH.

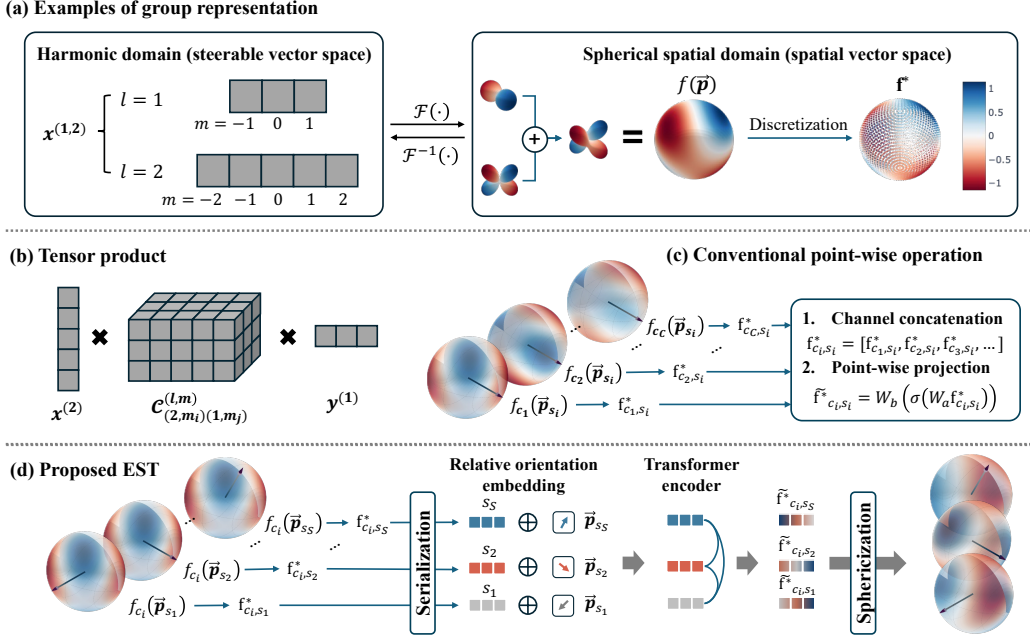


Figure 1: **Overview of operations in the spherical spatial domain.** (a) Examples of group representation. A Fourier transform is applied to project steerable vectors onto the spatial domain, which are then stored through sampling (i.e., discretization). (b) Tensor product operation. Steerable vectors are combined using the Clebsch-Gordan coefficient  $\mathcal{C}$ . (c) Conventional point-wise operation. All channels within the same orientation are processed by a vanilla neural network ((with linear projection  $W$  and activation  $\sigma(\cdot)$ ), and no interaction is performed across different orientations). (d) Proposed EST operation. A Transformer-based structure captures dependencies across all orientation pairs to model complex atomic behavior.

Density Functional Theory (DFT), GNNs can predict quantum properties in fractions of a second, significantly reducing computational cost from hours or days. Among the various GNN architectures, SE(3)-equivariant GNN [3, 4] has become a leading variant due to their inherent physical constraints, which can effectively capture intricate atomic interactions and address key challenges in molecular modeling.

In molecular systems, SE(3)-invariance and SE(3)-equivariance are fundamental constraints. For instance, molecular energies remain constant under rotation, while atomic forces rotate in concert with the molecule equivariantly. Early invariant models, such as SchNet [5] and HIP-NN [6], rely on interatomic distances in their message-passing blocks, consequently limiting their ability to capture interactions involving triplets or quadruplets of atoms [7]. Directional GNNs [8, 9] address this problem by explicitly incorporating bond angles and dihedral angles. While these models showed performance improvements, their expressiveness remains constrained due to a heavy reliance on handcrafted features. To capture deeper features, SE(3)-equivariant GNNs employ group representations as node embeddings and construct steerable message-passing blocks [3, 4, 10], where tensor product are applied to capture equivariant interactions between group embeddings (see Figure 1(b)). These GNNs achieve improved performance through end-to-end modeling, eliminating the need for hand-crafted features. Nevertheless, tensor product operations inherently suffer from limited non-linearity [3], and their expressiveness is bounded by the degree of group representations [11–13]. An alternative equivariant approach is to capture features in the spatial domain by applying a Fourier Transform (FT) to group representations, where embeddings are defined by square-integrable spherical functions (see the right side of Figure 1(a)). Prior works [14–16] typically apply simple point-wise neural networks to extract features from these spherical functions, operating independently on each orientation (see Figure 1(c)). However, **operations introducing non-linearity across different orientations in the spatial domain are rarely considered, as they risk violating equivariance. We demonstrate that this challenge can be overcome by subtly redesigning the FT sampling and architecture, which can also provide additional expressiveness** (Further analysis is provided in Section 3.2).

This paper presents the Equivariant Spherical Transformer (EST), a plug-and-play equivariant framework for high-fidelity modeling of atomic interactions. Our methodology initiates the process in the Fourier spatial domain of group representations by converting the spatial representation into a sequence of points. Subsequently, a Transformer-based architecture, as depicted in Figure 1(d), is employed to capture dependencies across different orientations on this sequence. A key finding of our work is that conventional spherical FT sampling methods, exemplified by the e3nn grid [17], significantly degrade equivariance. To mitigate this issue, we introduce a new, provably spherical sampling strategy grounded in the Fibonacci lattice, which we validate through theoretical and empirical analyses. Additionally, we incorporate a “hybrid mixture of experts” structure within our Transformer, featuring feed-forward networks in both the spatial and harmonic domains to strike an optimal balance between equivariance and model capacity. Experiments demonstrate that EST-based architectures attain state-of-the-art (SOTA) performance on standard benchmarks such as OC20 [18] and QM9 [19], with stable and notable improvements. On the complex molecular systems of the OC20 dataset, a compact EST model surpasses the performance of larger models and those leveraging external training data, thereby attesting to its strong expressiveness for modeling molecular systems.

**Our contributions are:** (i) We propose EST, a plug-and-play framework whose expressiveness subsumes that of traditional tensor products-based operations. (ii) We guarantee the equivariance of EST by subtly employing an approximately uniform sampling implementation on spherical FT. (iii) We demonstrate the superior performance of EST through extensive experiments. Furthermore, our ablation studies confirm the equivariance and enhanced expressiveness of EST, establishing it as a promising building block for a wide range of equivariant architectures.

## 2 Preliminaries and Related Work

In this section, we discuss related work and the corresponding mathematical background relevant to equivariant GNNs. We begin by listing the notations frequently used throughout the paper. We denote the unit sphere as  $\mathbb{S}^2$ , where the coordinate of a spherical point (or orientation)  $\vec{\mathbf{p}} = (\theta, \varphi)$  is represented by its polar angle  $\theta$  and azimuth angle  $\varphi$ . The symbol  $\mathbb{R}$  represents the set of real numbers, while  $\mathbf{R}$  denotes a rotation matrix for 3D vectors. We use  $[\cdot, \cdot]$  or  $\oplus$  to indicate tensor concatenation and  $\tilde{\cdot}$  to represent the update of tensors, respectively.

**Message Passing Neural Networks** Consider a graph  $\mathcal{G} = (\mathcal{V}, \mathcal{E})$ , with nodes  $v_i \in \mathcal{V}$  and edges  $e_{ij} \in \mathcal{E}$ . Each node  $v_i$  has an embedding  $\mathbf{x}_i$  and an attribute  $\mathbf{z}_i$ , and each edge  $e_{ij}$  has an attribute  $\mathbf{a}_{ij}$ . The Message Passing Neural Network (MPNN) [5], a specific type of GNN, updates node embeddings through a message block  $\mathbf{M}(\cdot)$  and an update block  $\mathbf{U}(\cdot)$  via the following steps:

$$\mathbf{m}_{ij} = \mathbf{M}(\mathbf{x}_i, \mathbf{x}_j, \mathbf{z}_i, \mathbf{z}_j, \mathbf{a}_{ij}, \vec{\mathbf{r}}_{ij}), \quad \text{and} \quad \tilde{\mathbf{x}}_i = \mathbf{U}(\mathbf{x}_i, \sum_{j \in \mathcal{N}(i)} \mathbf{m}_{ij}), \quad (1)$$

where we use  $\vec{\mathbf{r}}_{ij}$  to denote the relative position of node  $i$  and node  $j$  in 3D space, and the neighborhood  $\mathcal{N}(i)$  is typically defined by a cutoff radius:  $\mathcal{N}(i) = \{j \mid \|\vec{\mathbf{r}}_{ij}\| \leq r_{cut}\}$ . The node attribute  $\mathbf{z}_i$  contains atomic information such as the atomic type, and the edge attribute  $\mathbf{a}_{ij}$  contains atomic pair information such as distance and bond type. By stacking multiple message and update blocks, the final node embeddings can be used to model atomic interactions or represent molecular properties.

**Equivariance and Invariance** Given a group  $\mathbf{G}$  and a transformation parameter  $g \in \mathbf{G}$ , a function  $\phi : \mathcal{X} \rightarrow \mathcal{Y}$  is said to be equivariant to  $g$  if it satisfies:

$$\phi(T(g)[x]) = T'(g)[\phi(x)], \quad (2)$$

where  $T'(g) : \mathcal{Y} \rightarrow \mathcal{Y}$  and  $T(g) : \mathcal{X} \rightarrow \mathcal{X}$  denote the corresponding transformations on  $\mathcal{Y}$  and  $\mathcal{X}$ , respectively. Invariance is a special case of equivariance where  $T'(g)$  is the identity transformation. In this paper, we primarily focus on SO(3) equivariance, i.e., equivariance under 3D rotations, as it is closely related to the interactions between atoms in molecules<sup>4</sup>.

**Spherical Harmonics and Steerable Vectors** Spherical harmonics, a set of orthonormal basis functions defined over the sphere  $\mathbb{S}^2$ , are commonly employed in equivariant models. The real-valued spherical harmonics are typically denoted as  $\{Y^{(l,m)} : \mathbb{S}^2 \rightarrow \mathbb{R}\}$ ,

<sup>4</sup>Invariance under translation is trivially satisfied by using relative positions as inputs.

where  $l$  represents the degree and  $m$  represents the order. For any orientation  $\vec{\mathbf{p}}$ , we define  $\mathbf{Y}^{(l)}(\vec{\mathbf{p}}) = [Y^{(l,-l)}(\vec{\mathbf{p}}), Y^{(l,-l+1)}(\vec{\mathbf{p}}), \dots, Y^{(l,l)}(\vec{\mathbf{p}})]$ , a vector of size  $2l + 1$ , and  $\mathbf{Y}^{(0 \rightarrow l)}(\vec{\mathbf{p}}) = [\mathbf{Y}^{(0)}(\vec{\mathbf{p}}), \dots, \mathbf{Y}^{(l)}(\vec{\mathbf{p}})]$ , a vector of size  $(l + 1)^2$ .

A key property of spherical harmonics is their behavior under rotation  $\mathbf{R} \in SO(3)$ :

$$\mathbf{Y}^{(l)}(\mathbf{R}\vec{\mathbf{r}}) = \mathbf{D}^{(l)}(\mathbf{R})\mathbf{Y}^{(l)}(\vec{\mathbf{r}}), \quad (3)$$

where  $\mathbf{D}^{(l)}(\mathbf{R})$  is a  $(2l + 1) \times (2l + 1)$  matrix known as the Wigner-D matrix of degree  $l$ . Notably,  $\mathbf{D}^{(1)}(\mathbf{R}) = \mathbf{R}$ . Thus,  $\mathbf{R}$  and  $\mathbf{D}^{(l)}(\mathbf{R})$  can represent  $T(g)$  and  $T'(g)$  in (2). Following the convention in [20, 4], we say that  $\mathbf{Y}^{(l)}(\vec{\mathbf{p}})$  is steerable by the Wigner-D matrix of the same degree  $l$ . Furthermore, a vector that transforms according to an  $l$ -degree Wigner-D matrix is termed an  $l$ -degree steerable vector or a type- $l$  vector, residing in the vector space  $\mathbb{V}_l$ . Further mathematical details are available in Appendix A.1.

**Equivariant architectures** A common practice in equivariant models is to use steerable vectors as node embedding and encode relative positions  $\vec{\mathbf{r}}_{ij}$  using spherical harmonics as edge attributes. TFN [3] and NequIP [21] provide a general framework that learns the interaction between node embeddings and edge attributes through equivariant convolution filters. These filters are composed of equivariant operations such as degree-wise linear (DW-Linear) layers, Clebsch-Gordan (CG) tensor products, and Gate mechanisms. SEGNN [4] extends this convolution framework by more non-linear operations to achieve enhanced learning ability. SE(3)-Transformer [22] and Equiformer [10] introduce an attention mechanism that assigns rotation-invariant weights to edge attributes, thereby improving the learning of key atomic interactions. Nevertheless, the core operation in these works remains the convolution filter based on the CG tensor product. Additionally, GotenNet [23] proposes an effective and lightweight structure that separates steerable vectors into an  $l = 0$  invariant component and  $l > 0$  equivariant components, subsequently interacting these parts using inner products and scalar multiplication. In summary, due to the requirement of equivariance, most equivariant model architectures are constrained to specific equivariant operations. In this work, we transform the steerable vector into spherical spatial domain, enabling the application of more flexible and highly non-linear structures within message passing.

**Spherical Fourier Transform** Any square-integrable function  $f(\vec{\mathbf{p}})$  defined over the sphere  $\mathbb{S}^2$  can be expressed in a spherical harmonic basis via the spherical Fourier transform  $\mathcal{F}$ :

$$f(\vec{\mathbf{p}}) = \mathcal{F}(\mathbf{x}) = \sum_{l=0}^{\infty} \sum_{m=-l}^l x^{(l,m)} Y^{(l,m)}(\vec{\mathbf{p}}), \quad (4)$$

where  $x^{(l,m)}$  is the spherical Fourier coefficient. Conversely, the coefficient can be obtained from the function  $f(\vec{\mathbf{p}})$  via the inverse transform  $\mathcal{F}^{-1}$ :

$$x^{(l,m)} = \mathcal{F}^{-1}(f(\vec{\mathbf{p}})) = \int_{\Omega} f(\vec{\mathbf{p}}) Y^{(l,m)*}(\vec{\mathbf{p}}) d\Omega, \quad (5)$$

where  $d\Omega$  denotes the unit sphere and  $Y^{(l,m)*}(\cdot)$  is the conjugate of the spherical harmonic function. The function  $f(\vec{\mathbf{p}})$  and its coefficients  $\mathbf{x}$  are referred to as the representations in the spherical spatial domain and the harmonic domain, respectively. These processes are illustrated in Figure 1a. SCN [14] introduced an approach that applies a simple point-wise neural network in the spherical spatial domain. This technique has been subsequently adopted by several works [15, 16] within their message-passing frameworks. However, point-wise neural networks inherently limit their expressiveness. Our work aims to extend the capabilities of learning within the whole spherical spatial domain.

### 3 Model

In this section, we first make a review of tensor product to detail our motivation. Then, we introduction the formulation of our EST and clarify its properties.

### 3.1 Review of Clebsch-Gordan Tensor Product

A common approach in equivariant models is to incorporate steerable vectors with multiple degrees for node or edge features and then employing CG tensor products  $\otimes : \mathbb{V}_{l_1} \times \mathbb{V}_{l_2} \rightarrow \mathbb{V}_l$ , which is defined as:

$$(\mathbf{x}_1 \otimes \mathbf{x}_2)^{(l,m)} = \sum_{m_1=-l_1}^{l_1} \sum_{m_2=-l_2}^{l_2} C_{(l_1,m_1)(l_2,m_2)}^{(l,m)} \mathbf{x}_1^{(l_1,m_1)} \mathbf{x}_2^{(l_2,m_2)}, \quad (6)$$

where  $C_{(l_1,m_1)(l_2,m_2)}^{(l,m)}$  are the CG coefficients, a sparse tensor yielding non-zero terms when  $|l_1 - l_2| \leq l \leq (l_1 + l_2)$ . These products enable interactions between various combinations of  $l_1$  and  $l_2$ , crucial for the expressive power of MPNNs in representing latent equivariant functions [11, 12]. However, CG tensor products lack high non-linearities [4], often requiring the stacking of multiple layers to capture complex molecular features. Furthermore, their high computational complexity ( $\mathcal{O}(L^6)$ ) [24] makes architectures with stacked tensor product layers computationally expensive [4]. While techniques like Gate mechanisms [4, 10] and geometry-aware tensor attention [25] can be used to mitigate this limitation, they apply non-linear transformations to the invariant ( $l = 0$ ) representations. Higher-degree representations ( $l > 0$ ) are then updated through a unified scaling multiplication:

$$C_{inv} = \text{NL}(\mathbf{x}^{(0)}, \sum_{l=1}^L d(\mathbf{x}^{(l)})), \quad \text{and} \quad \tilde{\mathbf{x}}^{(l)} = C_{inv} \cdot \mathbf{x}^{(l)}, \quad (7)$$

where  $C_{inv}$  is an invariant scalar,  $\text{NL}(\cdot)$  is a non-linear network, and  $d(\cdot) : \mathbb{V}_l \rightarrow \mathbb{V}_0$  maps equivariant features to invariants, such as an inner product. This indirect exchange of information between higher-degree ( $l > 0$ ) representations still limits the overall expressiveness.

### 3.2 Equivariant Spherical Transformer

#### 3.2.1 Node embedding

**Steerable Representation** For representation with steerable vectors, we first define a maximal degree  $L$ . Each node  $n$ 's embedding  $\mathbf{x}_n$  comprises  $C$  channels, and each channel  $c$  is a concatenation of steerable vectors from degree 0 to  $L$ :  $\mathbf{x}_{n,c}^{(0 \rightarrow L)} = [x_{n,c}^{(0)}, \mathbf{x}_{n,c}^{(1)}, \dots, \mathbf{x}_{n,c}^{(L)}]$ . As a result, the dimension of a steerable node embedding is  $(L + 1)^2 \times C$ .

**Spatial Representation** Steerable representations  $\mathbf{x}_{n,c}$  can be transformed into a spherical function  $f_{n,c}(\vec{\mathbf{p}})$  via (4), with the summation truncated at a maximum degree  $L$ . Furthermore,  $f_{n,c}(\vec{\mathbf{p}})$  is discretely represented by sampling  $S$  points on the sphere, yielding a spatial node embedding  $\mathbf{f}_n^* \in \mathbb{R}^{S \times C}$ . It can be expressed as the concatenation over sampled points:

$$\mathbf{f}_{n,c}^* = [(\mathbf{x}_{n,c}^{(0 \rightarrow L)})^T \mathbf{Y}^{(0 \rightarrow L)}(\vec{\mathbf{p}}_1), (\mathbf{x}_{n,c}^{(0 \rightarrow L)})^T \mathbf{Y}^{(0 \rightarrow L)}(\vec{\mathbf{p}}_2), \dots, (\mathbf{x}_{n,c}^{(0 \rightarrow L)})^T \mathbf{Y}^{(0 \rightarrow L)}(\vec{\mathbf{p}}_S)]. \quad (8)$$

We use the term  $\mathbf{f}_{n,c,s}^*$  to denote the signal at the sampled point  $\vec{\mathbf{p}}_s$  of channel  $c$  of node  $n$ . The inverse transform in (5) can convert  $\mathbf{f}_n^*$  back to  $\mathbf{x}_n$ .

The steerable and spatial representations can be converted into each other. This property allows our proposed EST to be easily integrated as a plug-and-play module into a variety of equivariant models.

**The significance of operating in the spatial domain** In the spatial representation, the explicit degree and order are no longer directly accessible. Instead, higher-degree information is encoded as geometric features distributed across the spherical surface, as illustrated in Figure 1(a). Intuitively, by modeling the interdependencies of these geometric features, the model can effectively exchange information between implicit degrees, thereby approximating the capability of the tensor product discussed in Section 3.1. However, prior methods [14–16] only consider the feature dependencies across channels within the same sampling point (e.g.  $[\mathbf{f}_{c_1,s_1}^*, \mathbf{f}_{c_2,s_1}^*, \dots, \mathbf{f}_{c_C,s_1}^*]$ ), as depicted in Figure 1(c), overlooking geometric features composed of multiple points. In contrast, our proposed EST can model dependencies across various sampling points (e.g.  $[\mathbf{f}_{s_1}^*, \mathbf{f}_{s_2}^*, \dots, \mathbf{f}_{s_S}^*]$ ). We make two key claims: (i) our EST is SO(3)-equivariant by an uniform FL sampling strategy on the sphere, and (ii) its expressive power can surpass that of tensor product-based frameworks.

### 3.2.2 Spherical Attention

To prepare the data, we flatten all sampled points from  $\mathbf{f}^*$  into a sequential format, where each point  $s$  is represented by a  $C$ -dimensional feature vector. We then apply an attention mechanism [26]:

$$a_{s_i, s_j} = \frac{\exp(\mathbf{Q}_{s_i} \mathbf{K}_{s_j}^T / \sqrt{C})}{\sum_{s_k=1}^S \exp(\mathbf{Q}_{s_i} \mathbf{K}_{s_k}^T / \sqrt{C})}, \quad \text{and} \quad \tilde{\mathbf{f}}_{s_i}^* = \sum_{s_j=1}^S a_{s_i, s_j} \mathbf{V}_{s_j}, \quad (9)$$

where the  $\mathbf{Q}$ ,  $\mathbf{K}$ , and  $\mathbf{V}$  matrices are obtained through point-wise linear (PW-Linear) transformations of  $\mathbf{f}_{s_i}^*$ . The spherical attention is the core of EST. We also incorporate the pre-LayerNorm strategy [27] and feedforward networks (FFN) in EST. Our EST is applied in two ways: (i) for interactions between two spatial representations,  $\mathbf{Q}$  is derived from one, and  $\mathbf{K}$  and  $\mathbf{V}$  from the other; (ii) for learning features within a single spatial representation,  $\mathbf{Q}$ ,  $\mathbf{K}$ , and  $\mathbf{V}$  are all derived from it.

**Equivariance and sampling strategies** We demonstrate that the equivariance of the EST module is contingent upon the uniformity of the sampling points used in the FT. We begin with the following theorem:

**Theorem 1.** *Let  $\mathcal{P} = \{\vec{\mathbf{p}}_1, \dots, \vec{\mathbf{p}}_N\}$  be a set of sampled points used for the FT. The EST module is strictly  $SO(3)$ -equivariant if the set  $\mathcal{P}$  is closed under arbitrary rotations from the  $SO(3)$  group. That is, for any point  $\vec{\mathbf{p}}_i \in \mathcal{P}$  and any rotation  $\mathbf{R} \in SO(3)$ , there exists a point  $\vec{\mathbf{p}}_j \in \mathcal{P}$  such that  $\vec{\mathbf{p}}_j = \mathbf{R}\vec{\mathbf{p}}_i$ . In this case, the equivariance of EST property holds:*

$$\mathcal{F}^{-1}(\text{EST}(\mathcal{F}(\mathbf{D}\mathbf{x}))) = \mathbf{D}\mathcal{F}^{-1}(\text{EST}(\mathcal{F}(\mathbf{x}))), \quad (10)$$

where  $\mathbf{D}$  is an arbitrary Wigner-D rotation matrix.

The proof is provided in Appendix B.1. Due to the inherent symmetry of the sphere, a uniform sampling strategy can approximate the closed property of the point set  $\mathcal{P}$ , meaning a subset of rotations will satisfy  $\vec{\mathbf{p}}_j = \mathbf{R}\vec{\mathbf{p}}_i$ . In contrast, most prior works [15, 16] implement spherical FT using the e3nn library [17], which results in point densities that vary drastically with the polar angle  $\theta$  (see Figure 2(a) for visualization). To address this, we redefine the sampling implementation using Fibonacci Lattices (FL) [28]. The Cartesian coordinate of each sampling point  $s$  is defined by

$$\vec{\mathbf{p}}_s = [\sqrt{1 - z_s^2} \cos(2s\pi/\lambda), \sqrt{1 - z_s^2} \sin(2s\pi/\lambda), z_s], \quad (11)$$

where  $z_s = \frac{2s-1}{S-1}$  and  $\lambda = \frac{1+\sqrt{5}}{2}$  denotes the golden ratio. The (11) ensures the sampled points are distributed on the spherical surface, and different regions have similar densities (see Figure 2(b)). While FL sampling provides a high degree of uniformity, we further enhance this by simulating the points' motion on the sphere through consistent repulsions. This process, which resembles a simple molecular dynamics simulation, where each atom-like point is confined to the spherical surface, with forces determined by the distances between them.

The orthogonality of the basis functions in (4) is defined by  $\int_{\Omega} Y^{(l,m)}(\vec{\mathbf{p}}) Y^{(l',m')*}(\vec{\mathbf{p}}) d\Omega = \delta_{ll'} \delta_{mm'}$ , where  $\delta_{ij}$  is the Kronecker delta. Consequently, we redefine the implementation of the conjugate functions for the inverse FT as:

$$Y^{(l,m)*}(\vec{\mathbf{p}}) = \lambda^{(l,m)} Y^{(l,m)}(\vec{\mathbf{p}}), \quad (12)$$

where  $\lambda^{(l,m)} = 1 / \sum_s |Y^{(l,m)}(\vec{\mathbf{p}}_s)|^2$ . A detailed discussion comparing our sampling method with the e3nn implementation is provided in Appendix B.1. Furthermore, our ablation experiments (Table 5) demonstrate that sampling methods with poor uniformity can severely compromise equivariance.

**Expressiveness** As demonstrated by [11–13], the expressive power of CG tensor product-based frameworks is constrained by the maximum degree  $L$ , a finding corroborated by ablation experiments (Table 4). In contrast, our proposed EST module can project steerable representations of any degree onto the sphere and perform flexible, learnable operations. This allows the resulting features to be reprojected back to any desired degree, thereby potentially overcoming the expressiveness limitations of tensor products.

**Proposition 2.** *Under the assumption of no information loss in the spherical Fourier transform and its inverse, the function space spanned by the spherical Transformer encompasses that spanned by the CG tensor product.*

The detail is provided in Appendix B.2. We note that a spherical FT with no information loss is attainable by satisfying the Nyquist sampling rate, which mandates a minimum of  $(2L)^2$  sampling points on the sphere [14]. Thus, Proposition 2 validates the potential for substituting tensor products with EST. An empirical comparison of the expressiveness of EST and tensor product-based operations is presented in Section 4.3, where our EST significantly surpasses the upper bound of tensor products.

**Relative Orientation Embedding** In its basic form, spherical attention determines the dependencies between points based solely on their feature values, ignoring their relative positions in the input sequence. This means the output feature of a given point remains unchanged even if the order of all other points is altered. Such behavior is undesirable, as different point orderings correspond to distinct spherical functions. To enable the model to distinguish between these configurations, we introduce a relative orientation embedding by augmenting the query ( $\mathbf{Q}$ ) and key ( $\mathbf{K}$ ) vectors with orientation information:

$$\mathbf{Q}_{s_i} := [\mathbf{Q}_{s_i}, \vec{\mathbf{p}}_{s_i}], \quad \mathbf{K}_{s_j} := [\mathbf{K}_{s_j}, \vec{\mathbf{p}}_{s_j}], \quad \forall s_i, s_j \in \{1, 2, \dots, S\}. \quad (13)$$

Consequently, the inner product between  $\mathbf{Q}_{s_i}$  and  $\mathbf{K}_{s_j}$  now incorporates a term related to the orientation-aware inner product  $\vec{\mathbf{p}}_{s_i}^T \vec{\mathbf{p}}_{s_j}$ . Crucially, this augmentation does not compromise the equivariant inductive bias of EST, as proven in Appendix B.3. Our approach shares conceptual similarities with Rotary Position Embeddings (RoPE) in NLP [29], where the relative position embedding is invariant under transformation. However, our method fundamentally differs from RoPE by addressing rotation invariance instead of permutation invariance.

### 3.2.3 Mixture of Hybrid Experts

To enhance the model’s representational capacity, the FFNs in EST is reformed within a Mixture of Experts (MoE) framework [30]. Starting with the steerable representation  $\mathbf{x}$ , the invariant ( $l = 0$ ) component is used to compute expert weights through a gate function:

$$G(\mathbf{x}) = \text{Softmax}(\mathbf{x}^{(0)} \mathbf{W}_G), \quad (14)$$

where  $\mathbf{W}_G \in \mathbb{R}^{C \times E}$  is a trainable weight matrix. We then employ two distinct expert structures: (1) a steerable FFN, operating on steerable inputs and consisting of two DW-Linear layers with an intermediate Gate activation [10]; and (2) a spherical FFN, processing spatial inputs and comprising two PW-Linear layers with an intermediate SiLU activation [31]. The final output is a weighted combination of the outputs from these hybrid experts, with the weights determined by (14). These two expert types offer a crucial trade-off: the steerable FFN guarantees strict equivariance, while the spherical FFN provides enhanced expressive power. We therefore adapt their numbers based on the specific demands of the task. Further details and ablation studies can be found in Appendix C.

### 3.3 Applying the EST Module to Equivariant Models

We can apply EST module into equivariant models by two primary ways:

- **Message block:** We replace the conventional message block, often a tensor product like  $\text{Combine}(\mathbf{x}_i, \mathbf{x}_j) \otimes \vec{\mathbf{r}}_{ij}$ , with a EST. Here, the query ( $\mathbf{Q}$ ) is formed from a combination of the embeddings of nodes  $i$  and  $j$ , while the key ( $\mathbf{K}$ ) and value ( $\mathbf{V}$ ) are derived from the spherical harmonic representation of the relative position vector  $\vec{\mathbf{r}}_{ij}$ .
- **Update block:** To replace update block, all three attention components—query ( $\mathbf{Q}$ ), key ( $\mathbf{K}$ ), and value ( $\mathbf{V}$ )—are derived directly from the aggregated messages.

We provide an architecture in Appendix C.4 that uses the strategies mentioned above. Moreover, our approach leverages EST as a plug-and-play module that integrates seamlessly into existing equivariant models. Specifically, **we recommend replacing the standard update blocks—which require strong expressiveness to learn richer representations from complex aggregated message—with our EST-based update blocks.** This allows EST-based architectures to benefit from the computational efficiency and stability of existing message blocks while still enhancing their expressive power.

## 4 Experiments

In this section, we construct experiments to investigate the efficacy of the proposed method. We evaluate its performance on the S2EF/IS2RE tasks from the OC20 [18] benchmark and QM9 [19] tasks. Our analysis involves a comparison with a wide range of baseline models, including Schnet [5], PaiNN [32], SEGNN [4], TFN [3], Dimenet++ [33], Equiformer [10], Equiformerv2 [16] and EScAIP [34]. Specifically for the OC20 benchmark, we extend our comparison to include SpinConv [35], GemNet [9, 36], SphereNet [37], SCN [14] and eSCN [15]. Similarly, our QM9 experiments are augmented with comparisons to TorchMD-NET [38], EQGAT [39] and GotenNet [23]. The specific configurations employed for each baseline model can be found in Appendix D.1.

Table 1: S2EF validation results.  $\lambda_E$  is the coefficient of the energy loss. “only All” denotes training models with only S2EF-All dataset, and “All+MD” introduces additional OC20 MD dataset for training.

Model	Number of parameters	Throughput Samples/s	Energy MAE (meV) ↓	Force MAE (meV/Å) ↓
SchNet (only All)	9.1M	-	549	56.8
DimeNet++-L-F+E (only All)	10.7M	4.6	515	32.8
SpinConv (only All)	8.5M	6.0	371	41.2
GemNet-dT (only All)	32M	25.8	315	27.2
GemNet-OC (only All)	39M	18.3	244	21.7
SCN (20 layers, only All, test results)	271M	-	244	17.7
eSCN (20 layers, only All, test results)	200M	2.9	242	17.1
EScAIP-Small (All+MD)	83M	-	<b>229</b>	15.1
EquiformerV2 ( $\lambda_E = 4$ , 8 layers, All+MD)	31M	7.1	232	16.3
EquiformerV2 ( $\lambda_E = 2$ , 20 layers, only All)	153M	1.8	236	15.7
EST ( $\lambda_E = 4$ , 8 layers, only All)	45M	6.8	<b>229</b>	15.8
EST ( $\lambda_E = 2$ , 8 layers, only All)	45M	6.8	232	<b>15.0</b>

### 4.1 OC20 Results

**Dataset and Configurations** The OC20 dataset, comprising over 130 million molecular structures with force and energy labels, covers a broad spectrum of materials, surfaces, and adsorbates. We evaluate our models on two core sub-datasets of OC20: S2EF and IS2RE. All experimental configurations are detailed in Appendix D.2. Notably, We did not use very deep models or very long training schedules. For instance, our S2EF experiments utilize a 8-layer architecture, and IS2RE experiments employ a 6-layer one, significantly fewer than many advanced methods. Furthermore, as mentioned in Section 3.3, to enhance computational efficiency and facilitate a more direct comparison of different fundamental modules, we replace the EST architecture’s message module with the graph attention modules from EquiformerV2 and Equiformer for S2EF and IS2RE tasks, respectively.

**S2EF Results** We trained an 8-layer EST model on the S2EF-All dataset and evaluated its performance on the S2EF validation sets. Each validation set was divided into four similarly-sized subsets: ID, OOD Ads, OOD Cat, and OOD Both. Consistent with prior work [15, 16], the best model was selected based on its performance on the ID validation subset during training and subsequently evaluated across all validation subsets. For comparison with SCN and eSCN, we report their test results due to the absence of publicly available validation results; previous work [16] indicates that the validation and test sets have a similar distribution. We compared our results with two variants of the EquiformerV2 model: a deep 20-layer architecture and one trained with additional MD dataset. As shown in Table 1, EST outperformed both EquiformerV2 variants in energy and forces prediction. Furthermore, EST achieved competitive results in force prediction, surpassing several bigger baselines including EScAIP, SCN and eSCN.

**IS2RE Results** We trained our model directly on the IS2RE training set for energy prediction, without utilizing S2EF data. The results, summarized in Table 2, show that EST achieves SOTA performance on the ID, OOD Ads and OOD Both tasks and the second best on OOD Cat. Notably, the current SOTA models on OOD Cat, SCN, rely on complex 16-layer architectures with over

Table 2: IS2RE results of models trained on IS2RE training dataset. Bold and underline indicate the best result, and the second best result, respectively.

Model	Energy MAE (meV) ↓				EwT (%) ↑			
	ID	OOD Ads	OOD Cat	OOD Both	ID	OOD Ads	OOD Cat	OOD Both
SchNet	639	734	662	704	2.96	2.33	2.94	2.21
PaiNN	575	783	604	743	3.46	1.97	3.46	2.28
TFN	584	766	636	700	4.32	2.51	4.55	2.66
DimeNet++	562	725	576	661	4.25	2.07	4.10	2.41
GemNet-dT	527	758	549	702	4.59	2.09	4.47	2.28
GemNet-OC	560	711	576	671	4.15	2.29	3.85	2.28
SphereNet	563	703	571	638	4.47	2.29	4.09	2.41
SEGNN	533	692	537	679	<b>5.37</b>	2.46	4.91	2.63
Equiformer	504	688	521	630	5.14	2.41	4.67	2.69
SCN (16 layers)	516	<b>643</b>	530	604	4.92	<b>2.71</b>	4.42	<b>2.76</b>
EST (6 layers)	<b>501</b>	<u>652</u>	<b>502</b>	<b>578</b>	<u>5.16</u>	<u>2.67</u>	<b>5.16</b>	<b>2.76</b>

100M parameters. In contrast, EST employs a unified 6-layer structure comprising only 32.47M parameters, yet yields performance closely approaching theirs. Crucially, SCN relax equivariance to gain expressiveness, which can potentially lead to unstable predictions under input rotation. EST, conversely, provides more stable predictions owing to its stronger equivariance. Furthermore, in these IS2RE experiments, the EST architecture incorporates the message block from Equiformer. The key architectural difference resides in the update block. We observe that EST consistently surpasses the Equiformer model across all evaluated metrics, providing further evidence for the effectiveness of the proposed EST module and the model merging strategy discussed in Section 3.3.

Table 3: Results on QM9 dataset for various properties. † denotes using different data partitions.

Task	$\alpha$	$\Delta\varepsilon$	$\varepsilon_{HOMO}$	$\varepsilon_{LUMO}$	$\mu$	$C_v$	$G$	$H$	$R^2$	$U$	$U_0$	$ZPVE$
Units	$bohr^3$	meV	meV	meV	D	cal/(mol K)	meV	meV	$bohr^3$	meV	meV	meV
SchNet	.235	63	41	34	.033	.033	14	14	.073	19	14	1.70
TFN†	.223	58	40	38	.064	.101	-	-	-	-	-	-
DimeNet++	.044	33	25	20	.030	.023	8	7	.331	6	6	<b>1.21</b>
PaiNN	.045	46	28	20	.012	.024	7.35	<u>5.98</u>	<u>.066</u>	<b>5.83</b>	<u>5.85</u>	1.28
TorchMD-NET	.059	36	20	18	<u>.011</u>	.026	7.62	<u>6.16</u>	<b>.033</b>	6.38	<u>6.15</u>	1.84
SEGNN†	.060	42	24	21	.023	.031	15	16	.660	13	15	1.62
EQGAT	.053	32	20	<u>16</u>	<u>.011</u>	.024	23	24	.382	25	25	2.00
Equiformer	.046	30	15	14	<u>.011</u>	.023	7.63	6.63	.251	6.74	6.59	1.26
EquiformerV2	.050	<u>29</u>	<u>14</u>	<u>13</u>	<b>.010</b>	.023	7.57	6.22	.186	6.49	6.17	1.47
EST	.042	<b>28</b>	<b>13</b>	<b>12</b>	<u>.011</u>	<u>.022</u>	<b>7.03</b>	<b>5.94</b>	.298	5.92	<b>5.64</b>	1.31
EST (with GA)	<b>.041</b>	<u>29</u>	<u>14</u>	<u>13</u>	<u>.011</u>	<b>.021</b>	<u>7.18</u>	6.17	.227	<u>6.35</u>	6.32	1.27

## 4.2 QM9 Results

**Dataset and Configurations** The QM9 benchmark comprises quantum chemical properties for a relevant, consistent, and comprehensive chemical space of 134k equilibrium small organic molecules containing up to 29 atoms. Each atom is represented by its 3D coordinates and an embedding of its atomic type (H, C, N, O, F). We developed two model architectures: a 6-layer model employing the message-passing layer detailed in Figure 3, and a separate model that integrates message blocks (GA module) from Equiformer. For additional configuration specifics, please refer to Appendix D.2.

**Results** Given that the QM9 dataset is considerably smaller than OC20, models are more prone to overfitting if equivariance is destroyed. Ablation study in Table 5 shows that practical implementation for Fourier transform may lead to minor deviations from perfect equivariance. Nevertheless, EST and EST (with GA) achieve best on eight of the twelve tasks (see Table 3). Notably, EST (with GA) significantly outperformed Equiformer despite utilizing a similar message block. Furthermore, we included a comparison with GotenNet [25], which employs a more extensive training schedule. To ensure a fair assessment, we applied this schedule to EST as well; see Appendix D.3 for details.

### 4.3 Ablation study

In this section, we explore two key properties of EST: expressiveness and equivariance. The other experiments can be found in Appendix D, where we comprehensively investigate the influence of building components, including SA, spherical relative orientation embedding and hybrid experts.

Table 4: Experiments on Rotationally symmetric structures.

GNN Layer	2 fold	3 fold	10 fold	100 fold	GNN Layer	2 fold	3 fold	5 fold	10 fold
EST <sub>L=1</sub>	100.0 ± 0.0	100.0 ± 0.0	100.0 ± 0.0	100.0 ± 0.0	TFN/MACE <sub>L=1</sub>	50.0 ± 0.0	50.0 ± 0.0	50.0 ± 0.0	50.0 ± 0.0
EST <sub>L=2</sub>	100.0 ± 0.0	100.0 ± 0.0	100.0 ± 0.0	100.0 ± 0.0	TFN/MACE <sub>L=2</sub>	100.0 ± 0.0	50.0 ± 0.0	50.0 ± 0.0	50.0 ± 0.0
EST <sub>L=3</sub>	100.0 ± 0.0	100.0 ± 0.0	100.0 ± 0.0	100.0 ± 0.0	TFN/MACE <sub>L=3</sub>	100.0 ± 0.0	100.0 ± 0.0	50.0 ± 0.0	50.0 ± 0.0
EST <sub>L=5</sub>	100.0 ± 0.0	100.0 ± 0.0	100.0 ± 0.0	100.0 ± 0.0	TFN/MACE <sub>L=5</sub>	100.0 ± 0.0	100.0 ± 0.0	100.0 ± 0.0	50.0 ± 0.0
EST <sub>L=10</sub>	100.0 ± 0.0	100.0 ± 0.0	100.0 ± 0.0	100.0 ± 0.0	TFN/MACE <sub>L=10</sub>	100.0 ± 0.0	100.0 ± 0.0	100.0 ± 0.0	100.0 ± 0.0

**Expressiveness** Following [12], we employ evaluation metrics that distinguish  $n$ -fold symmetric structures to precisely assess EST’s expressive power. We first construct a single-layer message-passing layer based on Figure 3, consistent with tensor product-based operations (TFN, MACE). Additionally, we remove the steerable FFN for a clear comparison. As demonstrated in [11, 12], the expressive power of tensor product-based models is limited by the maximum degree  $L$ , failing to perfectly distinguish  $n$ -fold symmetric structures when  $n > L$ . From Table 4, we observe that EST significantly breaks through this theoretical boundary. It allows the model to distinguish symmetric structures even with very high fold (e.g., using 1-degree EST for 100-fold structures).

Table 5: Equivariance evaluation with different sampling strategies.

Sampling Strategy/Number	1-layer	2-layer	3-layer	4-layer	5-layer	6-layer
FL / $S = 64$ , w/o optim.	0.0010	0.0011	0.0010	0.0018	0.0022	0.004
FL / $S = 64$ , w optim.	0.0002	0.0001	0.0003	0.0003	0.0002	0.0002
FL / $S = 256$ , w/o optim.	0.0002	0.0002	0.0001	0.0002	0.0001	0.0003
e3nn / $S = 210$ , w/o optim.	0.0084	0.1006	0.0366	0.0593	0.0046	0.0199

**Equivariance** While we theoretically demonstrate that EST can achieve strict equivariance, perfect uniform sampling is challenging in practice, potentially leading to loss of equivariance. To investigate it, we build untrained networks with 1 to 6 layers based on a EST-only message passing, controlling the number of spherical sampling points and choosing whether to use molecular dynamics-like optimization. We randomly select 1000 molecules from QM9, compute their outputs  $y_1, \dots, y_{1000}$ , and then compute the outputs after applying random rotations,  $\hat{y}_1, \dots, \hat{y}_{1000}$ . The average absolute error  $(1/1000) \sum_{i=1}^{1000} |y_i - \hat{y}_i|$  serves as our measure. As shown in Table 5, EST with FL sampling closely approximates strict equivariance even without training, and its equivariance further improves with an increasing number of sampling points or a dynamics-like optimization. Additionally, we evaluated the equivariance error of 6-layer trained EST models on 1000 data samples from the each task of QM9 dataset. Across all properties, the average error was  $1.8 \times 10^{-5} \pm 0.7 \times 10^{-5}$ .

## 5 Conclusion

We present EST, a new SE(3)-equivariant framework for modeling molecules. By integrating a Transformer structure with steerable vectors, EST offers greater expressive power than tensor-product-based frameworks. We showed EST’s strong performance on the OC20 and QM9 datasets. A current limitation is the slight equivariance loss caused by spherical sampling. Future work will focus on improving spherical sampling uniformity. This could lead to better equivariance.

## References

- [1] Andrew W Senior, Richard Evans, John Jumper, James Kirkpatrick, Laurent Sifre, Tim Green, Chongli Qin, Augustin Žídek, Alexander WR Nelson, Alex Bridgland, et al. Improved protein structure prediction using potentials from deep learning. *Nature*, 577(7792):706–710, 2020.

- [2] C Lawrence Zitnick, Lowik Chanussot, Abhishek Das, Siddharth Goyal, Javier Heras-Domingo, Caleb Ho, Weihua Hu, Thibaut Lavril, Aini Palizhati, Morgane Riviere, et al. An introduction to electrocatalyst design using machine learning for renewable energy storage. *arXiv preprint arXiv:2010.09435*, 2020.
- [3] Nathaniel Thomas, Tess Smidt, Steven Kearnes, Lusann Yang, Li Li, Kai Kohlhoff, and Patrick Riley. Tensor field networks: Rotation-and translation-equivariant neural networks for 3d point clouds. *Neurips 2018*, 2018.
- [4] Johannes Brandstetter, Rob Hesselink, Elise van der Pol, Erik J Bekkers, and Max Welling. Geometric and physical quantities improve e (3) equivariant message passing. *The Tenth International Conference on Learning Representations*, 2022.
- [5] Kristof T Schütt, Huziel E Sauceda, P-J Kindermans, Alexandre Tkatchenko, and K-R Müller. SchNet—a deep learning architecture for molecules and materials. *The Journal of Chemical Physics*, 148(24):241722, 2018.
- [6] Nicholas Lubbers, Justin S Smith, and Kipton Barros. Hierarchical modeling of molecular energies using a deep neural network. *The Journal of chemical physics*, 148(24):241715, 2018.
- [7] Benjamin Kurt Miller, Mario Geiger, Tess E Smidt, and Frank Noé. Relevance of rotationally equivariant convolutions for predicting molecular properties. *arXiv preprint arXiv:2008.08461*, 2020.
- [8] Johannes Gasteiger, Janek Groß, and Stephan Günnemann. Directional message passing for molecular graphs. *ICLR2020*, 2020.
- [9] Johannes Gasteiger, Florian Becker, and Stephan Günnemann. Gemnet: Universal directional graph neural networks for molecules. *Advances in Neural Information Processing Systems*, 34:6790–6802, 2021.
- [10] Yi-Lun Liao and Tess Smidt. Equiformer: Equivariant graph attention transformer for 3d atomistic graphs. In *The Eleventh International Conference on Learning Representations*, 2023.
- [11] Nadav Dym and Haggai Maron. On the universality of rotation equivariant point cloud networks. In *International Conference on Learning Representations*, 2021.
- [12] Chaitanya K Joshi, Cristian Bodnar, Simon V Mathis, Taco Cohen, and Pietro Liò. On the expressive power of geometric graph neural networks. *arXiv preprint arXiv:2301.09308*, 2023.
- [13] Jiacheng Cen, Anyi Li, Ning Lin, Yuxiang Ren, Zihe Wang, and Wenbing Huang. Are high-degree representations really unnecessary in equivariant graph neural networks? *Advances in Neural Information Processing Systems*, 37:26238–26266, 2024.
- [14] C Lawrence Zitnick, Abhishek Das, Adeesh Kolluru, Janice Lan, Muhammed Shuaibi, Anuroop Sriram, Zachary Ulissi, and Brandon Wood. Spherical channels for modeling atomic interactions. *Neurips 2022*, 2022.
- [15] Saro Passaro and C Lawrence Zitnick. Reducing SO(3) convolutions to SO(2) for efficient equivariant gnns. volume 202 of *Proceedings of Machine Learning Research*, pages 27420–27438. PMLR, 2023.
- [16] Yi-Lun Liao, Brandon M Wood, Abhishek Das, and Tess Smidt. Equiformerv2: Improved equivariant transformer for scaling to higher-degree representations. In *The Twelfth International Conference on Learning Representations*, 2024.
- [17] Mario Geiger, Tess Smidt, Alby M., Benjamin Kurt Miller, Wouter Boomsma, Bradley Dice, Kostiantyn Lapchevskyi, Maurice Weiler, Michał Tyszkiewicz, Simon Batzner, Dylan Madiseti, Martin Uhrin, Jes Frellsen, Nuri Jung, Sophia Sanborn, Mingjian Wen, Josh Rackers, Marcel Rød, and Michael Bailey. Euclidean neural networks: e3nn, April 2022.
- [18] Lowik Chanussot, Abhishek Das, Siddharth Goyal, Thibaut Lavril, Muhammed Shuaibi, Morgane Riviere, Kevin Tran, Javier Heras-Domingo, Caleb Ho, Weihua Hu, et al. Open catalyst 2020 (oc20) dataset and community challenges. *ACS Catalysis*, 11(10):6059–6072, 2021.

- [19] Raghunathan Ramakrishnan, Pavlo O Dral, Matthias Rupp, and O Anatole Von Lilienfeld. Quantum chemistry structures and properties of 134 kilo molecules. *Scientific data*, 1(1):1–7, 2014.
- [20] Ines Chami, Zhitao Ying, Christopher Ré, and Jure Leskovec. Hyperbolic graph convolutional neural networks. *Advances in neural information processing systems*, 32, 2019.
- [21] Simon Batzner, Albert Musaelian, Lixin Sun, Mario Geiger, Jonathan P Mailoa, Mordechai Kornbluth, Nicola Molinari, Tess E Smidt, and Boris Kozinsky. E (3)-equivariant graph neural networks for data-efficient and accurate interatomic potentials. *Nature communications*, 13(1):1–11, 2022.
- [22] Fabian Fuchs, Daniel Worrall, Volker Fischer, and Max Welling. Se (3)-transformers: 3d roto-translation equivariant attention networks. *Advances in Neural Information Processing Systems*, 33:1970–1981, 2020.
- [23] Sarp Aykent and Tian Xia. Gotennet: Rethinking efficient 3d equivariant graph neural networks. In *The Thirteenth International Conference on Learning Representations (ICLR)*, 2025.
- [24] Shengjie Luo, Tianlang Chen, and Aditi S. Krishnapriyan. Enabling efficient equivariant operations in the fourier basis via gaunt tensor products. In *The Twelfth International Conference on Learning Representations (ICLR)*, 2024.
- [25] Sarp Aykent and Tian Xia. Gotennet: Rethinking efficient 3d equivariant graph neural networks. In *The Thirteenth International Conference on Learning Representations*, 2025.
- [26] Ashish Vaswani, Noam Shazeer, Niki Parmar, Jakob Uszkoreit, Llion Jones, Aidan N Gomez, Łukasz Kaiser, and Illia Polosukhin. Attention is all you need. *Advances in neural information processing systems*, 30, 2017.
- [27] Ruibin Xiong, Yunchang Yang, Di He, Kai Zheng, Shuxin Zheng, Chen Xing, Huishuai Zhang, Yanyan Lan, Liwei Wang, and Tieyan Liu. On layer normalization in the transformer architecture. In *International conference on machine learning*, pages 10524–10533, 2020.
- [28] Álvaro González. Measurement of areas on a sphere using fibonacci and latitude–longitude lattices. *Mathematical geosciences*, 42:49–64, 2010.
- [29] Jianlin Su, Murtadha Ahmed, Yu Lu, Shengfeng Pan, Wen Bo, and Yunfeng Liu. Roformer: Enhanced transformer with rotary position embedding. *Neurocomputing*, 568:127063, 2024.
- [30] Noam Shazeer, Azalia Mirhoseini, Krzysztof Maziarz, Andy Davis, Quoc Le, Geoffrey Hinton, and Jeff Dean. Outrageously large neural networks: The sparsely-gated mixture-of-experts layer. *arXiv preprint arXiv:1701.06538*, 2017.
- [31] Stefan Elfving, Eiji Uchibe, and Kenji Doya. Sigmoid-weighted linear units for neural network function approximation in reinforcement learning. *Neural networks*, 107:3–11, 2018.
- [32] Kristof Schütt, Oliver Unke, and Michael Gastegger. Equivariant message passing for the prediction of tensorial properties and molecular spectra. In *International Conference on Machine Learning*, pages 9377–9388. PMLR, 2021.
- [33] Johannes Klicpera, Shankari Giri, Johannes T Margraf, and Stephan Günnemann. Fast and uncertainty-aware directional message passing for non-equilibrium molecules. *arXiv preprint arXiv:2011.14115*, 2020.
- [34] Eric Qu and Aditi Krishnapriyan. The importance of being scalable: Improving the speed and accuracy of neural network interatomic potentials across chemical domains. *Advances in Neural Information Processing Systems*, 37:139030–139053, 2024.
- [35] Muhammed Shuaibi, Adeesh Kolluru, Abhishek Das, Aditya Grover, Anuroop Sriram, Zachary Ulissi, and C Lawrence Zitnick. Rotation invariant graph neural networks using spin convolutions. *arXiv preprint arXiv:2106.09575*, 2021.

- [36] Johannes Gasteiger, Muhammed Shuaibi, Anuroop Sriram, Stephan Günnemann, Zachary Ward Ulissi, C. Lawrence Zitnick, and Abhishek Das. Gemnet-OC: Developing graph neural networks for large and diverse molecular simulation datasets. *Transactions on Machine Learning Research*, 2022.
- [37] Yi Liu, Limei Wang, Meng Liu, Xuan Zhang, Bora Oztekin, and Shuiwang Ji. Spherical message passing for 3d graph networks. *ICLR2022*, 2021.
- [38] Philipp Thölke and Gianni De Fabritiis. Equivariant transformers for neural network based molecular potentials. In *International Conference on Learning Representations*, 2022.
- [39] Tuan Le, Frank Noé, and Djork-Arné Clevert. Equivariant graph attention networks for molecular property prediction. *arXiv preprint arXiv:2202.09891*, 2022.

## APPENDIX

<b>A</b>	<b>The Mathematics</b>	<b>14</b>
A.1	The Mathematics of Spherical Harmonics . . . . .	14
A.2	Equivariant Operation . . . . .	16
A.3	Relationship Between Expressive Power and Equivariant Operations . . . . .	18
<b>B</b>	<b>Proofs and Details For Section 3</b>	<b>18</b>
B.1	Proof for Equivariance of EST . . . . .	18
B.2	Expressiveness of EST . . . . .	20
B.3	Equivariance of Relative Orientation Embedding . . . . .	21
<b>C</b>	<b>Details of MoE</b>	<b>21</b>
C.1	Mixture of Experts in Language Models . . . . .	21
C.2	Mixture of Experts for Transformers . . . . .	21
C.3	Mixture of Hybrid Experts in EST . . . . .	22
C.4	Integration to Equivariant Architectures . . . . .	22
C.5	Ablation Studies . . . . .	22
<b>D</b>	<b>Details of Experiments and Supplementary Experiments</b>	<b>23</b>
D.1	Implementation Details of Baselines . . . . .	23
D.2	Implementation Details of EST Experiments . . . . .	23
D.3	Comparison between GotenNet and EST . . . . .	24
D.4	Supplementary Experiments . . . . .	25

### A The Mathematics

#### A.1 The Mathematics of Spherical Harmonics

##### A.1.1 The Properties of Spherical Harmonics

The spherical harmonics  $Y^{(l,m)}(\theta, \varphi)$  are the angular portion of the solution to Laplace’s equation in spherical coordinates where azimuthal symmetry is not present. Some care must be taken in identifying the notational convention being used. In this entry,  $\theta$  is taken as the polar (colatitudinal) coordinate with  $\theta$  in  $[0, \pi]$ , and  $\varphi$  as the azimuthal (longitudinal) coordinate with  $\varphi$  in  $[0, 2\pi)$ .

Spherical harmonics satisfy the spherical harmonic differential equation, which is given by the angular part of Laplace’s equation in spherical coordinates. If we define the solution of Laplace’s equation as  $F = \Phi(\varphi)\Theta(\theta)$ , the equation can be transformed as:

$$\frac{\Phi(\varphi)}{\sin \theta} \frac{d}{d\theta} \left( \sin \theta \frac{d\Theta}{d\theta} \right) + \frac{\Theta(\theta)}{\sin^2 \theta} \frac{d^2 \Phi(\varphi)}{d\varphi^2} + l(l+1)\Theta(\theta)\Phi(\varphi) = 0 \quad (15)$$

Here we omit the derivation process and just show the result. The (complex-value) spherical harmonics are defined by:

$$Y^{(l,m)}(\theta, \varphi) \equiv \sqrt{\frac{2l+1}{4\pi} \frac{(l-m)!}{(l+m)!}} P^{(l,m)}(\cos \theta) e^{im\varphi}, \quad (16)$$

where  $P^{(l,m)}(\cos \theta)$  is an associated Legendre polynomial. Spherical harmonics are integral basis, which satisfy:

$$\int_0^{2\pi} \int_0^\pi Y^{(l_1,m_1)}(\theta, \varphi) Y^{(l_2,m_2)}(\theta, \varphi) Y^{(l_3,m_3)}(\theta, \varphi) \sin \theta d\theta d\varphi = \sqrt{\frac{(2l_1+1)(2l_2+1)(2l_3+1)}{4\pi}} \begin{pmatrix} l_1 & l_2 & l_3 \\ 0 & 0 & 0 \end{pmatrix} \begin{pmatrix} l_1 & l_2 & l_3 \\ m_1 & m_2 & m_3 \end{pmatrix}, \quad (17)$$

where  $\begin{pmatrix} l_1 & l_2 & l_3 \\ m_1 & m_2 & m_3 \end{pmatrix}$  is a Wigner 3j-symbol (which is related to the Clebsch-Gordan coefficients). We list a few spherical harmonics which are:

$$\begin{aligned} Y^{(0,0)}(\theta, \varphi) &= \frac{1}{2} \sqrt{\frac{1}{\pi}}, \\ Y^{(1,-1)}(\theta, \varphi) &= \frac{1}{2} \sqrt{\frac{3}{2\pi}} \sin \theta e^{-i\varphi}, \\ Y^{(1,0)}(\theta, \varphi) &= \frac{1}{2} \sqrt{\frac{3}{\pi}} \cos \theta, \\ Y^{(1,1)}(\theta, \varphi) &= \frac{-1}{2} \sqrt{\frac{3}{2\pi}} \sin \theta e^{i\varphi}, \\ Y^{(2,-2)}(\theta, \varphi) &= \frac{1}{4} \sqrt{\frac{15}{2\pi}} \sin^2 \theta e^{-2i\varphi}, \\ Y^{(2,-1)}(\theta, \varphi) &= \frac{1}{2} \sqrt{\frac{15}{2\pi}} \sin \theta \cos \theta e^{-i\varphi}, \\ Y^{(2,0)}(\theta, \varphi) &= \frac{1}{4} \sqrt{\frac{5}{\pi}} (3 \cos^2 \theta - 1), \\ Y^{(2,1)}(\theta, \varphi) &= \frac{-1}{2} \sqrt{\frac{15}{2\pi}} \sin \theta \cos \theta e^{i\varphi}, \\ Y^{(2,2)}(\theta, \varphi) &= \frac{1}{4} \sqrt{\frac{15}{2\pi}} \sin^2 \theta e^{2i\varphi}, \end{aligned} \quad (18)$$

In this work, we use the real-value spherical harmonics rather than the complex-value one, which can be written as :

$$\begin{aligned} Y^{0,0}(\theta, \varphi) &= \sqrt{\frac{1}{4\pi}}, \\ Y^{(1,-1)}(\theta, \varphi) &= \sqrt{\frac{3}{4\pi}} \sin \varphi \sin \theta, \\ Y^{(1,0)}(\theta, \varphi) &= \sqrt{\frac{3}{4\pi}} \cos \theta, \\ Y^{(1,1)}(\theta, \varphi) &= \sqrt{\frac{3}{4\pi}} \cos \varphi \sin \theta, \\ Y^{(2,-2)}(\theta, \varphi) &= \sqrt{\frac{15}{16\pi}} \sin(2\varphi) \sin^2 \theta, \\ Y^{(2,-1)}(\theta, \varphi) &= \sqrt{\frac{15}{4\pi}} \sin \varphi \sin \theta \cos \theta, \\ Y^{(2,0)}(\theta, \varphi) &= \sqrt{\frac{5}{16\pi}} (3 \cos^2 \theta - 1), \\ Y^{(2,1)}(\theta, \varphi) &= \sqrt{\frac{15}{4\pi}} \cos \varphi \sin \theta \cos \theta, \\ Y^{(2,2)}(\theta, \varphi) &= \sqrt{\frac{15}{16\pi}} \cos(2\varphi) \sin^2 \theta. \end{aligned} \quad (19)$$

### A.1.2 Fourier transformation over $\mathbb{S}^2$

In the main paper, we show that any square-integrable function  $f(\cdot)$  can thus be expanded as a linear combination of spherical harmonics:

$$f(\vec{\mathbf{p}}) = \sum_{l=0}^{\infty} \sum_{m=-l}^l \mathbf{x}^{(l,m)} Y^{(l,m)}(\vec{\mathbf{p}}), \quad (20)$$

where  $\vec{\mathbf{p}} = (\theta, \varphi)$  denotes the orientations, like what we do in the main paper. The coefficient  $\mathbf{x}^{(l,m)}$  can be obtained by the inverse transformation over  $\mathbb{S}^2$ , which is

$$\mathbf{x}^{l,m} = \int_{\Omega} f(\vec{\mathbf{p}}) Y^{(l,m)*}(\vec{\mathbf{p}}) d\Omega = \int_0^{2\pi} d\varphi \int_0^{\pi} d\theta \sin \theta f(\vec{\mathbf{p}}) Y^{(l,m)*}(\vec{\mathbf{p}}). \quad (21)$$

Using the fact  $\mathbf{Y}^l(\mathbf{R}\vec{\mathbf{p}}) = \mathbf{D}^l(\mathbf{R})\mathbf{Y}^l(\vec{\mathbf{p}})$ , and (20), we know

$$f(\mathbf{R}\vec{\mathbf{p}}) = \sum_{l=0}^{\infty} \sum_{m=-l}^l \mathbf{x}^{(l,m)} Y^{(l,m)}(\mathbf{R}\vec{\mathbf{p}}) = \sum_{l=0}^{\infty} \sum_{m=-l}^l \mathbf{x}^{(l,m)} \mathbf{D} Y^{(l,m)}(\vec{\mathbf{p}}). \quad (22)$$

Therefore, we can get the conclusion that spatial representation  $f(\mathbf{R}\vec{\mathbf{P}})$  and  $f(\vec{\mathbf{P}})$  is steerable, which can be represented by

$$f(\mathbf{R}\vec{\mathbf{p}}) = \mathbf{D}^{-1} \mathbf{x} = \mathbf{D}^T \mathbf{x}. \quad (23)$$

### A.1.3 The Relationship Between Spherical Harmonics and Wigner-D Matrix

A rotation  $\mathbf{R}$  sending the  $\vec{\mathbf{p}}$  to  $\mathbf{R}\vec{\mathbf{p}}$  can be regarded as a linear combination of spherical harmonics that are set to the same degree. The coefficients of linear combination represent the complex conjugate of an element of the Wigner D-matrix. The rotational behavior of the spherical harmonics is perhaps their quintessential feature from the viewpoint of group theory. The spherical harmonics  $Y^{l,m}$  provide a basis set of functions for the irreducible representation of the group  $\text{SO}(3)$  with dimension  $(2l+1)$ .

The Wigner-D matrix can be constructed by spherical harmonics. Consider a transformation  $Y^{l,m}(\vec{\mathbf{p}}) = Y^{l,m}(\mathbf{R}_{\alpha,\beta,\gamma}\vec{\mathbf{p}}_x)$ , where  $\vec{\mathbf{p}}_x$  denote the x-orientation.  $\alpha, \beta, \gamma$  denotes the items of Euler angle. Therefore,  $Y^{l,m}(\vec{\mathbf{p}})$  is invariant with respect to rotation angle  $\gamma$ . Based on this viewpoint, the Wigner-D matrix with shape  $(2l+1) \times (2l+1)$  can be defined by:

$$\mathbf{D}^{(l,m)}(\mathbf{R}_{\alpha,\beta,\gamma}) = \sqrt{2l+1} Y^{(l,m)}(\vec{\mathbf{p}}). \quad (24)$$

In this case, the orientations are encoded in spherical harmonics and their Wigner-D matrices, which are utilized in our cross module.

## A.2 Equivariant Operation

### A.2.1 Equivariance of Clebsch-Gordan Tensor Product

The Clebsch-Gordan Tensor Product shows a strict equivariance for different group representations, which make the mixture representations transformed equivariant based on Wigner-D matrices. We use  $\mathbf{D}^{l,m'm}$  to denote the element of Wigner-D matrix in the degree  $l$ . The Clebsch-Gordan coefficient satisfies:

$$\begin{aligned} & \sum_{m'_1, m'_2} \mathcal{C}_{(l_1, m'_1)(l_2, m'_2)}^{(l_0, m_0)} \mathbf{D}^{(l_1, m'_1 m_1)}(g) \mathbf{D}^{(l_2, m'_2 m_2)}(g) \\ &= \sum_{m'_0} \mathbf{D}^{(l_0, m'_0 m_0)}(g) \mathcal{C}_{(l_1, m_1)(l_2, m_2)}^{(l_0, m'_0)} \end{aligned} \quad (25)$$

Therefore, the spherical harmonics can be combined equivariantly by CG Tensor Product:

$$\begin{aligned}
& CG \left( \sum_{m'_1} \mathbf{D}^{(l_1, m_1 m'_1)}(g) Y^{(l_1, m'_1)}, \sum_{m'_2} \mathbf{D}^{(l_2, m_2 m'_2)}(g) Y^{(l_2, m'_2)} \right) \\
&= \sum_{m_1, m_2} C_{(l_1, m_1)(l_2, m_2)}^{(l_0, m_0)} \sum_{m'_1} \mathbf{D}^{(l_1, m_1 m'_1)}(g) Y^{(l_1, m'_1)} \sum_{m'_2} \mathbf{D}^{(l_2, m_2 m'_2)}(g) Y^{(l_2, m'_2)} \\
&= \sum_{m'_0} \mathbf{D}^{(l_0, m_0 m'_0)}(g) \sum_{m_1, m_2} C_{(l_1, m_1)(l_2, m_2)}^{(l_0 m'_0)} Y^{(l_1, m'_1)} Y^{(l_2, m'_2)} \\
&= \sum_{m'_0} \mathbf{D}^{(l_0, m_0 m'_0)}(g) CG \left( Y^{(l_1, m'_1)}, Y^{(l_2, m'_2)} \right).
\end{aligned} \tag{26}$$

Here, we omit the input argument of the spherical harmonics, which can represent any direction on the sphere. (26) represents a relationship between scalar. If we transform the scalar to vector or matrix like what we do in (3), (26) is equal to

$$(\mathbf{D}^{l_1} \mathbf{u} \otimes \mathbf{D}^{l_2} \mathbf{v})^{l_0} = \mathbf{D}^{l_0} (\mathbf{u} \otimes \mathbf{v})^{l_0}. \tag{27}$$

The tensor CG product mixes two representations to a new representation under special rule  $|l_1 - l_2| \leq l \leq (l_1 + l_2)$ . For example, 1. two type-0 vectors will only generate a type-0 representations; 2. type- $l_1$  and type- $l_2$  can generate type- $l_1 + l_2$  vector at most. Note that some widely-used products are related to tensor product: scalar product ( $l_1 = 0, l_2 = 1, l = 1$ ), dot product ( $l_1 = 1, l_2 = 1, l = 0$ ) and cross product ( $l_1 = 1, l_2 = 1, l = 1$ ). However, for each element with  $l > 0$ , there are multi mathematical operation for the connection with weights. The relation between number of operations and degree is quadratic. Thus, as degree increases, the amount of computation increases significantly, making calculation of the CG tensor product slow for higher order irreps. This statement can be proven by the implementation of e3nn (o3.FullyConnectedTensorProduct).

### A.2.2 Learnable Parameters in Tensor Product

Previous works utilize the e3nn library [17] to implement the corresponding tensor product. It is crucial to emphasize that the formulation of CG tensor product is devoid of any learnable parameters, as CG coefficients remain constant. In the context of e3nn, learnable parameters are introduced into each path, represented as  $w(\mathbf{u}^{l_1} \otimes \mathbf{v}^{l_2})$ . Importantly, these learnable parameters will not destroy the equivariance of each path. However, they are limited in capturing directional information. In equivariant models, the original CG tensor product primarily captures directional information. We have previously mentioned our replacement of the CG tensor product with learnable modules. It is worth noting that our focus lies on the CG coefficients rather than the learnable parameters in the e3nn implementation.

### A.2.3 Gate Activation and Normalization

**Gate Activation.** In equivariant models, the Gate activation combines two sets of group representations. The first set consists of scalar steerable vector ( $l = 0$ ), which are passed through standard activation functions such as sigmoid, ReLU and SiLU. The second set comprises higher-order steerable vector ( $l > 0$ ), which are multiplied by an additional set of scalar steerable vector that are introduced solely for the purpose of the activation layer. These scalar steerable vector are also passed through activation functions.

**Normalization.** Normalization is a technique commonly used in neural networks to normalize the activations within each layer. It helps stabilize and accelerate the training process by reducing the internal covariate shift, which refers to the change in the distribution of layer inputs during training.

The normalization process involves computing the mean and variance across the channels. In equivariant normalization, the variance is computed using the root mean square value of the L2-norm of each type- $l$  vector. Additionally, this normalization removes the mean term. The normalized activations are then passed through a learnable affine transformation without a learnable bias, which enables the network to adjust the mean and variance based on the specific task requirements.

### A.3 Relationship Between Expressive Power and Equivariant Operations

In [11], Theorem 2 establishes the universality of equivariant networks based on the TFN structure:

**Theorem.** For all  $n \in \mathbb{N}$ ,  $l_T \in \mathbb{N}_+^*$ ,

- 1. For  $D \in \mathbb{N}_+$ , every G-equivariant polynomial  $p : \mathbb{R}^{3 \times n} \rightarrow W_{l_T}^n$  of degree  $D$  is in  $F_{C(D), D}^{TFN}$ .
- 2. Every continuous G-equivariant function can be approximated uniformly on compact sets by functions in  $\cup_{D \in \mathbb{N}_+} F_{C(D), D}^{TFN}$ .

Here,  $n$  represents the number of input points (or nodes),  $l_T$  represents the degree of the approximated G-equivariant function,  $C$  represents the number of channels, and  $D$  represents the degree of the TFN (Tensor Field Network) structure, which is equivalent to the term  $l$  used in our method. The TFN structure consists of two layers, including convolution and self-interaction. Self-interaction involves equivariant linear functions. The convolution operation calculates the CG tensor product between different steerable representations, which is a fundamental operation for transforming directional information. Most equivariant models based on group representations use a similar approach (CG tensor product) to capture directional features. Therefore, the theorem mentioned above also applies to building blocks based on CG tensor products, such as SEGNN [4] and Equiformer [10].

It is important to note that achieving an infinite degree in practice is not feasible. However, equivariant models based on group representations can enhance their expressive power by increasing the number of maximal degrees [11]. In their evaluation of expressive power, as presented in [12], the authors utilize the GWL (geometric Weisfeiler-Leman) graph isomorphism test. In Table 2 of their work, it is evident that equivariant models with a maximal degree denoted as  $L$  are incapable of distinguishing  $n$ -fold symmetric structures when  $n$  exceeds the value of  $L$ .

## B Proofs and Details For Section 3

### B.1 Proof for Equivariance of EST

The proof for Theorem 1 is shown in the following.

*Proof.* Recall that FT can be represented by

$$f(\vec{\mathbf{p}}) = \sum_{l=0}^L \sum_{m=-l}^l x^{(l,m)} Y^{(l,m)}(\vec{\mathbf{p}}) = (\mathbf{x}^{(0 \rightarrow L)})^T \mathbf{Y}^{(0 \rightarrow L)}(\vec{\mathbf{p}}). \quad (28)$$

When we apply a random rotation  $\mathbf{D}^{-1}$  to  $\mathbf{x}$ , we obtain

$$(\mathbf{D}^{-1} \mathbf{x}^{(0 \rightarrow L)})^T \mathbf{Y}^{(0 \rightarrow L)}(\vec{\mathbf{p}}) \quad (29)$$

$$= (\mathbf{x}^{(0 \rightarrow L)})^T \mathbf{D} \mathbf{Y}^{(0 \rightarrow L)}(\vec{\mathbf{p}}) \quad (30)$$

$$= (\mathbf{x}^{(0 \rightarrow L)})^T \mathbf{Y}^{(0 \rightarrow L)}(\mathbf{R} \vec{\mathbf{p}}) \quad (31)$$

$$= f(\mathbf{R} \vec{\mathbf{p}}), \quad (32)$$

where  $\mathbf{R}$  and  $\mathbf{D}$  share the same transformation parameters.

Given a spatial representation  $f(\vec{\mathbf{p}})$  transformed from a steerable representation  $\mathbf{x}$ , spherical attention can be represented as:

$$\tilde{f}(\vec{\mathbf{p}}_1) = \int_{\vec{\mathbf{p}}_2 \in \Omega} a(f^Q(\vec{\mathbf{p}}_1), f^K(\vec{\mathbf{p}}_2)) f^V(\vec{\mathbf{p}}_2) d\vec{\mathbf{p}}_2, \quad (33)$$

where  $a(\cdot)$  denotes the operation to compute attention coefficients. Terms  $Q, K, V$  denote three independent linear transformations. When the origin representation  $\mathbf{x}$  is rotation by a Wigner-D matrix  $\mathbf{D}^{-1}$ , the representation  $f(\vec{\mathbf{p}})$  is transformed to  $f(\mathbf{R} \vec{\mathbf{p}})$ . Therefore, the attention results are

changed to

$$\begin{aligned}
& \int_{\mathbf{R}\vec{\mathbf{p}}_2 \in \Omega} a(f^Q(\mathbf{R}\vec{\mathbf{p}}_1), f^K(\mathbf{R}\vec{\mathbf{p}}_2)) f^V(\mathbf{R}\vec{\mathbf{p}}_2) d\mathbf{R}\vec{\mathbf{p}}_2 \\
&= \int_{\mathbf{R}\vec{\mathbf{p}}_2 \in \Omega} \frac{\exp(f^Q(\mathbf{R}\vec{\mathbf{p}}_1) * f^K(\mathbf{R}\vec{\mathbf{p}}_2))}{\int_{\mathbf{R}\vec{\mathbf{p}}_3 \in \Omega} \exp(f^Q(\mathbf{R}\vec{\mathbf{p}}_1) * f^K(\mathbf{R}\vec{\mathbf{p}}_3)) d\mathbf{R}\vec{\mathbf{p}}_3} f^V(\mathbf{R}\vec{\mathbf{p}}_2) d\mathbf{R}\vec{\mathbf{p}}_2 \\
&= \int_{\mathbf{R}\vec{\mathbf{p}}_2 \in \Omega} \frac{\exp(f^Q(\mathbf{R}\vec{\mathbf{p}}_1) * f^K(\mathbf{R}\vec{\mathbf{p}}_2))}{\int_{\vec{\mathbf{p}}_3 \in \Omega} \exp(f^Q(\mathbf{R}\vec{\mathbf{p}}_1) * f^K(\vec{\mathbf{p}}_3)) d\vec{\mathbf{p}}_3} f^V(\mathbf{R}\vec{\mathbf{p}}_2) d\mathbf{R}\vec{\mathbf{p}}_2 \quad (34) \\
&= \int_{\vec{\mathbf{p}}_2 \in \Omega} \frac{\exp(f^Q(\mathbf{R}\vec{\mathbf{p}}_1) * f^K(\vec{\mathbf{p}}_2))}{\int_{\vec{\mathbf{p}}_3 \in \Omega} \exp(f^Q(\mathbf{R}\vec{\mathbf{p}}_1) * f^K(\vec{\mathbf{p}}_3)) d\vec{\mathbf{p}}_3} f^V(\vec{\mathbf{p}}_2) d\vec{\mathbf{p}}_2 \\
&= \int_{\vec{\mathbf{p}}_2 \in \Omega} a(f^Q(\mathbf{R}\vec{\mathbf{p}}_1), f^K(\vec{\mathbf{p}}_2)) f^V(\vec{\mathbf{p}}_2) d\vec{\mathbf{p}}_2 \\
&= \tilde{f}(\mathbf{R}\vec{\mathbf{p}}_1).
\end{aligned}$$

Therefore, the output of spherical attention remains steerable after rotation. If we transform  $\tilde{f}(\mathbf{R}\vec{\mathbf{p}}_1)$  into its steerable representation, denoted as  $\tilde{\mathbf{x}}$ , the following relationship holds:

$$\tilde{\mathbf{x}} = \mathbf{D}^{-1} \mathcal{F}^{-1}(\text{SA}(\mathcal{F}(\mathbf{x}))) = \mathcal{F}^{-1}(\text{SA}(\mathcal{F}(\mathbf{D}^{-1}\mathbf{x}))) \quad (35)$$

The equivariance of spherical attention holds. Moreover, the spherical FFNs is obviously equivariant because the function  $\tilde{f}(\vec{\mathbf{p}}_1) = \text{FFN}(f(\vec{\mathbf{p}}_1))$  only focus on one orientation. Therefore, we can prove that the whole EST framework contained spherical attention and spherical FFN is equivariant.  $\square$

Note that (34) rely on continuous sphere, i.e closed set of orientations  $\vec{\mathbf{p}}$ . In the implementation, the continuous function must be represented by discrete sampling. The attention operation become

$$\tilde{f}(\vec{\mathbf{p}}_1) = \sum_{\vec{\mathbf{p}}_2} a(f^Q(\vec{\mathbf{p}}_1), f^K(\vec{\mathbf{p}}_2)) f^V(\vec{\mathbf{p}}_2). \quad (36)$$

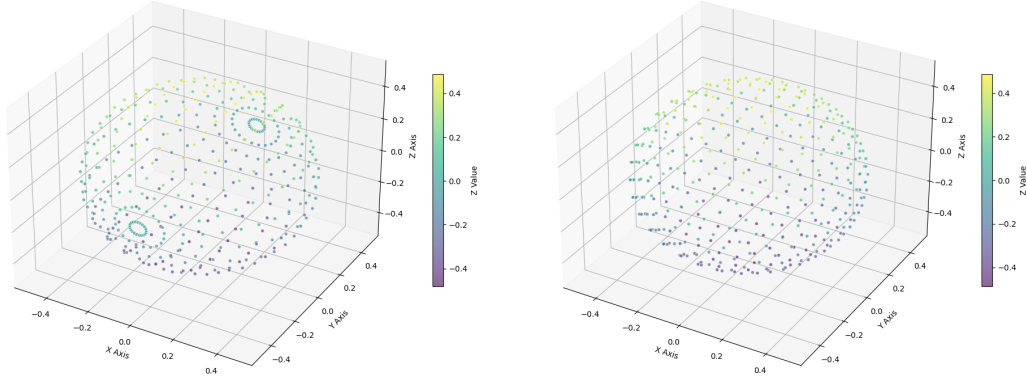
After introducing random rotations, (36) becomes

$$\tilde{f}(\mathbf{R}\vec{\mathbf{p}}_1) = \sum_{\vec{\mathbf{p}}_3} a(f^Q(\mathbf{R}\vec{\mathbf{p}}_1), f^K(\vec{\mathbf{p}}_3)) f^V(\vec{\mathbf{p}}_3). \quad (37)$$

Let us consider an ideal case where the point density is the same across all local regions. That is, the points on the sphere are perfectly uniformly distributed. The entire sphere is symmetric. The set of  $\vec{\mathbf{p}}_1$ ,  $\vec{\mathbf{p}}_2$ , and  $\vec{\mathbf{p}}_3$  all come from a set of sampling points. For this set, if one point  $\vec{\mathbf{p}}_i$  can be mapped to another point  $\vec{\mathbf{p}}_j$  through a specific rotation  $\mathbf{R}$ , then the other points can also find their corresponding points through this rotation due to perfect symmetry. In this case, we say that the set of sampling points is closed under a special subset of rotations. The model is strictly equivariant on these special rotations.

**Sampling strategies** Most previous works use the e3nn implementation for spherical Fourier transform. However, it significantly destroy the uniformity of spherical sampling, which is illustrated in Figure 2(a). In contrast, Fibonacci Lattices (FL) do not directly divide the polar angle and azimuth angle into a grid. Instead, they select sampling points on the sphere in a spiral pattern. As shown in Figure 2(b), FL tends to achieve more uniform sampling, thereby improving the equivariance of EST. This is also consistent with the results observed in Table 5.

**Enhanced Uniformity** Building on the FL sampling, we further propose a scattering optimization strategy similar to molecular dynamics. We define a distance-based interaction force between every two points: the greater the distance, the smaller the force. Then, we iterate two processes: 1. Simultaneously optimize the three-dimensional coordinates of all points through the interaction forces; 2. Re-project all points back onto the sphere. After multiple rounds of iteration, the spherical sampling points can become more uniform. It is worth noting that both the FL sampling and the dynamics simulation are conducted during the model initialization phase. Once we obtain the uniform sampling points, we save their results and directly read them in the model’s feedforward process.



(a) e3nn Sampling

(b) Fibonacci Lattices Sampling

Figure 2: Two spherical sampling strategies.

## B.2 Expressiveness of EST

In Proposition 2, we claim that the function space spanned by the spherical Transformer encompasses that spanned by the CG tensor product and give an intuitive explanation. Here, we provide a mathematical explanation for further understanding.

Given two steerable vectors  $\mathbf{u} \in \mathbb{V}_{0 \rightarrow l_1}$  and  $\mathbf{v} \in \mathbb{V}_{0 \rightarrow l_2}$ , and we define the CG tensor product result is  $\mathbf{w} \in \mathbb{V}_{l_0}$ , where  $l_0 \leq l_1 + l_2$ . The spatial representations of  $\mathbf{w}$  can be represented as:

$$\sum_{l_0, m_0} \mathbf{w}^{(l_0, m_0)} Y^{(l_0, m_0)} = \sum_{l_0, m_0} (\mathbf{u}^{(0 \rightarrow l_1)})^T \mathbf{C}_{(0 \rightarrow l_1), (0 \rightarrow l_2)}^{(l_0, m_0)} \mathbf{v}^{(0 \rightarrow l_2)} Y^{(l_0, m_0)}, \quad (38)$$

where  $\mathbf{C}_{(0 \rightarrow l_1), (0 \rightarrow l_2)}^{(l_0, m_0)}$  is a matrix including the whole CG coefficients corresponding to degree  $l_0$  and order  $m_0$ . We temporarily ignore the input of the spherical harmonics. The spherical Transformer use the multiplication between spatial representations of  $\mathbf{u}$  and  $\mathbf{v}$ :

$$\begin{aligned} & \sum_{l_1, m_1} \mathbf{u}^{(l_1, m_1)} Y^{(l_1, m_1)} \sum_{l_2, m_2} \mathbf{v}^{(l_2, m_2)} Y^{(l_2, m_2)} \\ &= \sum_{l_1, m_1, l_2, m_2} \mathbf{u}^{(l_1, m_1)} Y^{(l_1, m_1)} \mathbf{v}^{(l_2, m_2)} Y^{(l_2, m_2)} \\ &= \mathbf{u}^{(0 \rightarrow l_1)T} (\mathbf{Y}^{(0 \rightarrow l_1)T} \mathbf{Y}^{(0 \rightarrow l_2)}) \mathbf{v}^{(0 \rightarrow l_2)} \end{aligned} \quad (39)$$

Recall that CG coefficients are in fact the expansion coefficients of a product of two spherical harmonics in terms of a single spherical harmonic (see (17)):

$$Y^{(l_1, m_1)} Y^{(l_2, m_2)} = \sum_{l_0, m_0} \sqrt{\frac{(2l_1 + 1)(2l_2 + 1)}{4\pi(2l_0 + 1)}} \mathcal{C}_{(l_1, m_1)(l_2, m_2)}^{(0, 0)} \mathcal{C}_{(l_1, m_1)(l_2, m_2)}^{(l_0, m_0)} Y^{l_0, m_0}, \quad (40)$$

(39) can be transformed to

$$\begin{aligned} & \mathbf{u}^{(0 \rightarrow l_1)T} (\mathbf{Y}^{(0 \rightarrow l_1)T} \mathbf{Y}^{(0 \rightarrow l_2)}) \mathbf{v}^{(0 \rightarrow l_2)} \\ &= \sum_{l_0, m_0} \mathbf{u}^{(0 \rightarrow l_1)T} \mathbf{H}_{(0 \rightarrow l_1), (0 \rightarrow l_2)}^{(l_0, m_0)} \mathbf{v}^{(0 \rightarrow l_2)} Y^{(l_0, m_0)}, \end{aligned} \quad (41)$$

where  $\mathbf{H}_{(l_1, m_1), (l_2, m_2)}^{(l_0, m_0)} = \sqrt{\frac{(2l_1 + 1)(2l_2 + 1)}{4\pi(2l_0 + 1)}} \mathcal{C}_{(l_1, m_1)(l_2, m_2)}^{(0, 0)} \mathcal{C}_{(l_1, m_1)(l_2, m_2)}^{(l_0, m_0)}$ . Compared to  $\mathbf{C}_{(0 \rightarrow l_1), (0 \rightarrow l_2)}^{(l_0, m_0)}$ , the term  $\mathbf{H}_{(0 \rightarrow l_1), (0 \rightarrow l_2)}^{(l_0, m_0)}$  introduces an additional constant term that can be approximated by linear layers and the FFNs. Therefore, (39) is equivalent to (38). On the other hand, (39) is inherently part of the Transformer architecture: when relationships between different orientations are masked and the  $\mathbf{V}$  vectors are taken as constant vectors, the Transformer can naturally reduce to (39).

Through the above process, we find that the spherical representation of the output from the CG tensor product is fundamentally a special case of EST. Furthermore, *EST can capture dependencies between different orientations, which is particularly beneficial for approximating higher degree spherical harmonic representations. For instance, at a orientation  $(\theta, \varphi)$ , higher-degree spherical harmonics may involve contributions from other orientations such as  $(2\theta, \varphi)$ ,  $(\theta, 2\varphi)$ ,  $(2\theta, 2\varphi)$  (see  $Y^{(2)}$  in (19)). The Transformer in EST can directly combine these lower-degree terms in these orientations to approximate the higher-order terms at the orientation  $(\theta, \varphi)$ .*

### B.3 Equivariance of Relative Orientation Embedding

The equivariance of relative orientation embedding can be easily proven with the same way in (34), where  $a(f^Q(\mathbf{R}\vec{\mathbf{p}}_1), f^K(\mathbf{R}\vec{\mathbf{p}}_2))$  is transformed to

$$\frac{\exp(f^Q(\mathbf{R}\vec{\mathbf{p}}_1) * f^K(\mathbf{R}\vec{\mathbf{p}}_2) + (\mathbf{R}\vec{\mathbf{p}}_1)^T(\mathbf{R}\vec{\mathbf{p}}_2))}{\int_{\mathbf{R}\vec{\mathbf{p}}_3 \in \Omega} \exp(f^Q(\mathbf{R}\vec{\mathbf{p}}_1) * f^K(\mathbf{R}\vec{\mathbf{p}}_3) + (\mathbf{R}\vec{\mathbf{p}}_1)^T(\mathbf{R}\vec{\mathbf{p}}_3)) d\mathbf{R}\vec{\mathbf{p}}_3}. \quad (42)$$

Due to the spherical symmetry, we can still eliminate the rotation  $\mathbf{R}$  acting on  $\mathbf{p}_2$  and  $\mathbf{p}_3$ . Therefore, after incorporating the Relative Orientation Embedding, EST retains its equivariance.

## C Details of MoE

### C.1 Mixture of Experts in Language Models

Recently, empirical evidence consistently demonstrates that increased model parameters and computational resources yield performance gains in language models when sufficient training data is available. However, scaling models to extreme sizes incurs prohibitive computational costs. The Mixture-of-Experts (MoE) architecture has emerged as a promising solution to this dilemma. By enabling parameter scaling while maintaining moderate computational requirements, MoE architectures have shown particular success when integrated with Transformer frameworks. These implementations have successfully scaled language models to substantial sizes while preserving performance advantages.

### C.2 Mixture of Experts for Transformers

We begin with a standard Transformer language model architecture, which comprises  $Y$  stacked Transformer blocks:

$$\mathbf{u}^y = \text{Self-Att}(\mathbf{h}^{m-1}) + \mathbf{h}^{m-1}, \quad (43)$$

$$\mathbf{h}^y = \text{FFN}(\mathbf{u}^y) + \mathbf{u}^y, \quad (44)$$

where  $\text{Self-Att}(\cdot)$  denotes the self-attention module,  $\text{FFN}(\cdot)$  denotes the Feed-Forward Network (FFN),  $\mathbf{u}^y$  are the hidden states of all tokens after the  $y$ -th attention module, and  $\mathbf{h}^y \in \mathbb{R}^d$  is the output hidden state after the  $y$ -th Transformer block. layer normalization is omitted for brevity. The MoE architecture substitutes FFN layers in Transformers with MoE layers and each MoE layer comprises multiple structurally identical experts. Each token is dynamically assigned to several experts based on learned routing probabilities: If the  $y$ -th FFN is substituted with an MoE layer, the computation for its output hidden state  $\mathbf{h}^y$  can be expressed as:

$$\mathbf{h}^y = \sum_{i=1}^N (g_i \text{FFN}_i(\mathbf{u}^y)) + \mathbf{u}^y, \quad (45)$$

$$g_i = \begin{cases} s_i, & s_i \in \text{Topk}(\{s_j | 1 \leq j \leq N\}, K), \\ 0, & \text{otherwise,} \end{cases} \quad (46)$$

$$s_i = \text{Softmax}_i \left( (\mathbf{u}^y)^T \mathbf{e}_i^y \right), \quad (47)$$

where  $N$  denotes the total number of experts,  $\text{FFN}_i(\cdot)$  is the  $i$ -th expert FFN,  $g_i$  denotes the gate value for the  $i$ -th expert,  $s_i$  denotes the token-to-expert affinity,  $\text{Topk}(\cdot, K)$  denotes the set comprising  $K$  highest affinity scores among those calculated for all  $N$  experts, and  $\mathbf{e}_i^y$  is the learnable parameters

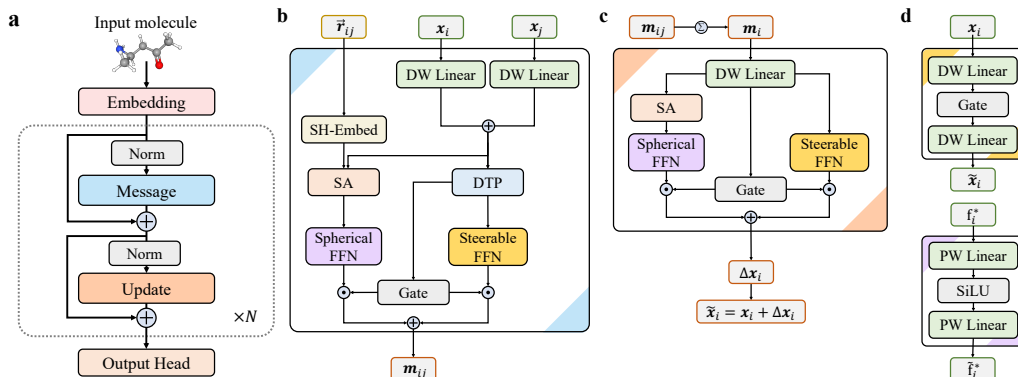


Figure 3: **The architecture and building blocks of EST.** SH and DTP denote spherical harmonic embedding and depth-wise tensor product [10], respectively. For simplicity, the Fourier and inverse Fourier transform steps are omitted. (a) Overall architecture. (b) Message block. (c) Update block. (d) Two experts operating on the steerable and spatial representations, respectively.

representing the centroid of the  $i$ -th expert in the  $y$ -th layer. The sparsity property ( $K \ll N$ ) ensures computational efficiency by restricting each token to interact with only  $K$  experts.

### C.3 Mixture of Hybrid Experts in EST

Inspired by MoE of language models, we developed the mixture of hybrid experts for EST. Its computation can be expressed as:

$$\tilde{\mathbf{m}} = \sum_{i=1}^{N_{steerable}} (g_i \text{SteerableFFN}_i(\mathbf{m})) + \sum_{j=1}^{N_{spherical}} (g_j \text{SphericalFFN}_j(\mathbf{m})) + \mathbf{m}, \quad (48)$$

$$g_i = \begin{cases} s_i, & s_i \in \text{Topk}(\{s_k | 1 \leq k \leq N_{steerable}\}, K), \\ 0, & \text{otherwise,} \end{cases} \quad (49)$$

$$g_j = \begin{cases} s_j, & s_j \in \text{Topk}(\{s_k | 1 \leq k \leq N_{spherical}\}, K), \\ 0, & \text{otherwise,} \end{cases} \quad (50)$$

$$s_i, s_j = \text{split} \left( \text{Softmax} \left( \mathbf{m}^{(0)} \mathbf{W} \right) \right), \quad (51)$$

where  $\mathbf{m}$  and  $\tilde{\mathbf{m}}$  denote the input and output message, respectively,  $\mathbf{m}^{(0)}$  denotes the invariant part of message,  $\mathbf{W} \in \mathbb{R}^{C \times (N_{steerable} + N_{spherical})}$  represents the learnable expert centroids. Here, we omit the symbol of layer order for simplicity.

### C.4 Integration to Equivariant Architectures

EST with MoE can be employed both in the message block to compute edge features and in the update block to refine node embeddings. Figure 3(b,c) defines a message passing layer with EST. When computing the message, the  $\mathbf{Q}$  in SA come from the aggregation of node  $i$  and  $j$  embeddings, while  $\mathbf{K}$  and  $\mathbf{V}$  is derived from the spherical harmonic representation of the relative position  $\tilde{\mathbf{r}}_{ij}$ . In the SA of the update block,  $\mathbf{Q}$ ,  $\mathbf{K}$ , and  $\mathbf{V}$  are all derived from the aggregated message. Additionally, in the message and update blocks shown in Figure 3, the spatial expert is used after spherical attention, and the steerable expert is employed as a parallel branch. They are combined using gate weights.

### C.5 Ablation Studies

In terms of MoE, there are three key hyper-parameters, including expert count, routing sparsity (top-K), and load balancing. Our ablation studies begin with the easiest steerable MoE using the QM9 dataset and Equiformer baseline.

- **Expert count:** We assessed model performance across expert counts ranging from 1 to 64. Performance improved up to 10 experts, reaching optimal results at that point (Table 6). Meanwhile, excessive expert count leads to a significant increase in time cost while the improvement in performance may not necessarily continue. In contrast, setting the number of expert as 10 offers the right balance between performance improvement and time cost.
- **Routing Sparsity:** We evaluated different levels of sparsity by varying the K values in the top-K router, while increased sparsity (lower K values) degraded performance (Table 7).
- **Load Balancing:** The auxiliary balance loss was added to the training loss with varying ratios (0 to 0.1). However, introducing balance loss consistently reduced model performance (Table 8).

The discrepancy between our findings and typical language model observations regarding sparsity and balancing can be attributed to several factors. While sparsity and balancing mechanisms generally enhance efficiency in standard language models, the limited size of the QM9 dataset plays a crucial role in this divergence. Introducing more experts increases model complexity, which can lead to overfitting rather than improved generalization, particularly when training data is scarce. Furthermore, given our limited number of experts, the necessity for stringent sparsity enforcement and elaborate load balancing mechanisms is diminished. In such scenarios, employing a dense MoE configuration tends to yield optimal performance.

Table 6: Performance and time cost depending on expert count when predicting  $\alpha$  on QM9.

Number of experts	1(w/o MoE)	2	4	8	10	16	32	64
Test MAE (bohr <sup>3</sup> )	0.0466	0.0461	0.0503	0.0437	<b>0.0424</b>	0.0449	0.0438	0.0443
Time per epoch (s)	373.69	391.93	416.53	472.80	500.71	576.01	893.20	1664.93

Table 7: Effect of routing sparsity for predicting  $\alpha$  on QM9.

K	2	3	5	10 (Dense)
Test MAE (bohr <sup>3</sup> )	0.04338	0.04349	0.04472	<b>0.0424</b>

Table 8: Impact of balance loss ratio for predicting  $\alpha$  on QM9.

Ratio	0 (w/o balance loss)	0.001	0.01	0.1
Test MAE (bohr <sup>3</sup> )	<b>0.0424</b>	0.04369	0.04369	0.04361

## D Details of Experiments and Supplementary Experiments

### D.1 Implementation Details of Baselines

In the S2EF experiment, the results of baselines in Table 1 follow [16], where each model is trained in official configuration. Most of these configurations can be found in Fairchem repository, and we also follow its code framework to construct our OC20 experiments. In the IS2RE experiment, the results in Table 2 of baselines follow [10] and [14]. In the QM9 experiment, the results in Table 3 of baselines follow [16] and [23].

### D.2 Implementation Details of EST Experiments

**S2EF and IS2RE** In our experiments on OC20, we adopt two hybrid models: S2EF combines the message module from EquiformerV2 with the update module of EST, while IS2RE combines the message module of Equiformer with the update module of EST. To ensure a fair comparison, all training configurations are aligned with those of the original EquiformerV2 and Equiformer. The hyperparameters specific to the EST architecture include the number of spherical sampling points, the number and dimension of experts in the steerable FFN, and the number of experts in the spherical

Table 9: Hyper-parameters for the EST model setting on OC20 S2EF and OC20 IS2RE experiments.

Hyper-parameters	S2EF-ALL	IS2RE
Optimizer	AdamW	AdamW
Learning rate scheduling	Cosine learning rate with linear warmup	Cosine learning rate with linear warmup
Warmup epochs	0.01	2
Maximum learning rate	$4 \times 10^{-4}$	$2 \times 10^{-4}$
Batch size	256	32
Number of epochs	4	20
Weight decay	$1 \times 10^{-3}$	$1 \times 10^{-3}$
Dropout rate	0.1	0.2
Energy coefficient $\lambda_E$	4, 2	1
Force coefficient $\lambda_F$	100	-
Gradient clipping norm threshold	100	100
Model EMA decay	0.999	0.999
Cutoff radius ( $\text{\AA}$ )	12	5
Maximum number of neighbors	20	500
Number of radial bases	600	128
Dimension of hidden scalar features in radial functions	128	64
Maximum degree $L_{max}$	6	1
Maximum order $M_{max}$	2	1
Number of Layers	8	6
Node embedding dimension	128	(256, $l = 0$ ), (128, $l = 1$ )
Intermediate dimension during the Fourier transform	128	256
Intermediate dimension and the number of steerable FFN	128, 6	[(768, $l = 0$ ), (384, $l = 1$ )], 5
Intermediate dimension and the number of spherical FFN	512, 4	512, 5
Number of spherical point samples	128	128

FFN. Detailed configurations for all models are summarized in Table 9. The experiment on S2EF is conducted on 32 NVIDIA A100 GPUs and the experiment on S2EF is conducted on 8 NVIDIA A100 GPUs.

Table 10: Hyper-parameters for QM9 dataset.

Hyper-parameters	EST-based model (Figure 3)	EST (with GA)
Optimizer	AdamW	AdamW
Learning rate scheduling	Cosine learning rate with linear warmup	Cosine learning rate with linear warmup
Warmup steps	5	5
Maximum learning rate	$5 \times 10^{-4}, 2 \times 10^{-4}$	$5 \times 10^{-4}, 1.5 \times 10^{-4}$
Batch size	128, 64	128, 64
Max training epochs	350, 700	300, 600
Weight decay	$5 \times 10^{-3}, 0$	$5 \times 10^{-3}, 0$
Dropout rate	0.0, 0.2	0.0, 0.2
Number of radial bases	128 for Gaussian radial basis 8 for radial Bessel basis	
Cutoff radius ( $\text{\AA}$ )	5	5
$L_{max}$	2	2
Number of layers	6	6
Node dimension	128	(128, $l = 0$ ), (64, $l = 1$ ), (32, $l = 2$ )
Spherical harmonics embedding dimension	(1, $l = 0$ ), (1, $l = 1$ ), (1, $l = 2$ )	(1, $l = 0$ ), (1, $l = 1$ ), (1, $l = 2$ )
Intermediate dimension during the Fourier transform	128	128
Intermediate dimension and the number of steerable FFN	5, 128	6, (768, $l = 0$ ), (384, $l = 1$ )
Intermediate dimension and the number of spherical FFN	5, 512	4, 512
Number of spherical point samples	200, 128	128

**QM9** In the QM9 experiments, we design two EST variants: 1) a fully EST-based architecture with both message and update blocks; 2) a hybrid model combining the message block of Equiformer and the update block of EST. To ensure a fair comparison with state-of-the-art methods (Equiformer and EquiformerV2), we adopt similar configurations as shown in Table 10. Note that Equiformer employs two different configurations for the following properties:  $\alpha, \Delta\varepsilon, \varepsilon_{\text{HOMO}}, \varepsilon_{\text{LUMO}}, \mu, C_v, R^2, \text{ZPVE}$ , and  $G, H, U, U_0$ . We follow the same strategy in our experiments. Comparisons with another SOTA model, GotenNet [23], are conducted under different configurations, and the details are provided in Section D.3.

### D.3 Comparison between GotenNet and EST

Comparing with GotenNet, a variant of EST was designed incorporating the GATA message block and substituting the original updating block with our proposed mixture of hybrid experts. The steerable

part of the hybrid expert maintain the architecture of EQFF in GotenNet, while the EST updating module serves as the spherical part used in parallel. To maintain a lightweight design, we simply integrate one steerable expert with one spherical expert. Our model adopts the same number of layers as GotenNet but achieves better performance across 8 tasks (table 11). In addition, to ensure a fair comparison, we use training configurations similar to those of the original GotenNet (see Table 12), including a batch size of 32 and a training schedule of 1000 epochs. *It is notable that several training hyper-parameters of EST differ from those used of GotenNet. For example, GotenNet specifies 10,000 warm-up steps, whereas our model sets this to 0. Additionally, we employed MAE as the loss function, while MSE was used for GotenNet instead.*

Notably, these target properties can be broadly categorized into energy-related variables (e.g.,  $G, H, U, U_0$ , etc.) and molecular geometry-related variables (e.g.,  $\alpha, \mu$ , etc.). We further observed that these two categories of properties exhibit different convergence characteristics during training, which aligns with previous work [4]. Specifically, the energy-related properties are more sensitive to hyperparameters such as the optimizer and learning rate schedule, while the geometry-related properties are relatively less sensitive. Given this, we divided the properties into two groups and tuned different training hyperparameters for each group (see Table 12). It is worth noting that GotenNet has already achieved low error levels on these properties, meaning the scope for further improvement is quite limited.

Table 11: Results on QM9 dataset for various properties.

Task	$\alpha$	$\Delta\varepsilon$	$\varepsilon_{HOMO}$	$\varepsilon_{LUMO}$	$\mu$	$C_v$	$G$	$H$	$R^2$	$U$	$U_0$	ZPVE
Units	$bohr^3$	meV	meV	meV	D	cal/(mol K)	meV	meV	$bohr^3$	meV	meV	meV
GotenNet (4 layers)	.033	<b>21.2</b>	16.9	13.9	.0075	.020	5.50	<b>3.70</b>	<b>0.029</b>	<b>3.67</b>	3.71	<b>1.09</b>
EST (4 layers with GATA)	<b>.030</b>	31.2	<b>16.7</b>	<b>13.3</b>	<b>.0070</b>	<b>.019</b>	<b>5.40</b>	3.71	<b>0.029</b>	3.70	<b>3.70</b>	1.19

Table 12: Hyper-parameters for the EST (with GATA) models on QM9 experiments.

Hyper-parameters	EST (with GATA)	
properties	$\alpha, \Delta\varepsilon, \varepsilon_{HOMO}, \varepsilon_{LUMO}, \mu, C_v, R^2$	$G, H, U, U_0, U, ZPVE$
Loss function	MAE	MSE
Warmup steps	0	10000
Weight decay	0	0.01
Intermediate dimension and the number of steerable FFN	512, 1	512, 4
Intermediate dimension and the number of spherical FFN	512, 1	512, 4
Learning rate scheduling	linear warmup with reduce on plateau	
Optimizer	AdamW	
Maximum learning rate	$1 \times 10^{-4}$	
Batch size	32	
Max training epochs	1000	
Dropout rate	0.1	
Number of RBFs	64	
Cutoff radius (Å)	5	
Lmax	2	
Number of layers	4	
Node dimension	256	
Edge dimension	256	
Number of attention heads	8	
Number of spherical point samples	64	

#### D.4 Supplementary Experiments

**Building Blocks** We conducted ablation studies to validate the effectiveness of individual building blocks within EST. Specially, in Table 13, removing the steerable FFN means all experts are replaced by the spherical FFN, removing the spherical FFN means all experts are replaced by the steerable FFN and removing FL Sampling refers to using the Fourier transform from e3nn instead. We used the prediction of the  $\alpha$  property on QM9 as the core task for evaluation. As shown in Table 13, all components positively contribute to the overall performance. We draw several conclusions:

1. The **SA module with layer normalization** effectively improves overall performance.
2. **Mixing steerable and spherical experts** helps strike a balance between equivariance and expressive power, leading to better generalization performance.

3. **FL Sampling is crucial for EST.** Disrupting equivariance without it significantly harms the results on QM9.

Table 13: Ablation studies for modules in HDGNN.

Building blocks in EST					$\alpha$ MAE
LayerNorm	SA	Steerable FFN	Spherical FFN	FL Sampling	<i>bohr</i> <sup>3</sup>
-	✓	✓	✓	✓	0.046
-	-	✓	✓	✓	0.044
✓	✓	-	✓	✓	0.045
-	-	✓	-	✓	0.042
✓	✓	✓	✓	-	0.053
✓	✓	✓	✓	✓	<b>0.041</b>